Low-Frequency Variability in the Mid-Latitude Atmosphere Induced by an Oceanic Thermal Front

Yizhak Feliks[1], Michael Ghil[2, 3], and Eric Simonnet[4]

Department of Atmospheric Sciences and Institute of Geophysics and Planetary Physics, University of California, Los Angeles, CA 90095-1567

J. Atmos. Sci., submitted

October 28, 2002

[1]*Permanent address*: Mathematics Department, Israel Institute of Biological Research, Nes-Ziona, Israel

[2]*Corresponding author*; E-mail: ghil@atmos.ucla.edu

[3]*Additional address*: Département Terre-Atmosphère-Océan and Laboratoire de Météorologie Dynamique, Ecole Normale Supérieure, Paris, France

[4]*Permanent address*: Institut Non-Linéaire de Nice**,** CNRS, Nice, France

Abstract

This study examines the flow induced in a simple atmospheric model by an east–west oriented oceanic thermal front. The model has a linear marine boundary layer coupled to a quasi-geostrophic, equivalent-barotropic free atmosphere. An eastward jet, parallel to the oceanic front's isotherms, characterizes the flow induced in the free atmosphere by the vertical velocity at the top of the boundary layer. A large gyre develops on either side of this jet, cyclonic to the north and anticyclonic to the south of it. As the jet intensifies during spin-up from rest, it becomes unstable. The most unstable wave has a length of about 500 km, it evolves into a meander, and eddies detach from the eastern edge of each gyre.

The dependence of the atmospheric dynamics on the strength T_* of the oceanic front is studied. The Gulf Stream and Kuroshio fronts correspond roughly, in our scaling, to $T_* \approx 7$ °C. For weak fronts, $T_* \leq 4$ °C, the circulation is steady and exhibits two large, antisymmetric gyres separated by a westerly zonal jet. As the front strengthens, $4 < T_* < 5$, the solution undergoes Hopf bifurcation to become periodic in time, with a period of 30 days, and spatially asymmetric. The bifurcation is due to the westerly jet's barotropic instability, which has a symmetric spatial pattern. This pattern's being added to the antisymmetric mean results in the overall asymmetry of the full solution. The spatial scale and amplitude of the symmetric, internally generated, as well as the antisymmetric, forced mode both increase with the strength T_* of the oceanic front. For $T_* \geq 5$ °C the solution becomes chaotic, but a dominant period still stands out above the broadband noise. This dominant period increases with T_*, overall, but the increase is not monotonic.

The oceanic front's intensity dictates the mean speed of the atmospheric jet. Two energy regimes are obtained: (i) In the low-energy regime, the SST front and hence the atmospheric jet are weak; in this regime small meanders develop along the jet axis, and the dominant period is about 30 days. (ii) In the high-energy regime, the SST front and the jet are strong; in it large meanders and eddies develop along the jet, and the dominant oscillation has a period of about 70 days. The physical nature of the two types of oscillations is discussed, as are possible transitions between them when T_* changes on very long time scales.

1. Introduction

Over the last two decades, the response of the atmospheric marine boundary layer (AMBL) to oceanic fronts has been studied in observations, as well as by analytical and numerical models (Sweet et al. 1981; Businger and Shaw 1984; Hsu 1987; Rogers 1989; Warner et al. 1990; Doyle and Warner 1990, 1993; Giordani and Planton 2000). These studies have shown that the AMBL reaches heights of 600–1200 m, with the greater height lying over the warm side of the front. The potential temperature gradient of the induced atmospheric front in many cases extends up to the top of the AMBL. The vertical velocity at the top of the AMBL right above the front's axis reaches values of several cms^{-1}, while the horizontal wind along the front has a speed of several ms^{-1}. The maximum wind speed is colocated with the pressure gradient maximum.

The circulation in the AMBL adjusts to changes in the oceanic-surface conditions in several hours. In the case of very strong fronts, as observed in the GALE program (Doyle and Warner 1990), intense and narrow jets have been measured, whose speeds exceed $20ms^{-1}$. Superimposed on the jets were short waves, of 50–90 km, and small atmospheric eddies. These waves and eddies have been attributed to barotropic instability induced by the horizontal shear (Doyle and Warner 1993).

The most prominent inhomogeneity in ocean surface properties is the thermal contrast across major oceanic currents and upwelling zones. Mid-oceanic thermal fronts, such as the Gulf Stream and Kuroshio Extension, are permanent features of the mid-latitude ocean circulation. These fronts change in position and strength on the time scale of weeks to years. The sea-surface temperature (SST) difference across these fronts is of about (4–10 °C)/(100 km). Most of the data on these fronts are derived from a limited number of in situ hydrographic sections and a much larger number of remotely taken, satellite infrared images (Lee and Cornillon 1996).

There are thus two types of atmospheric low-frequency variability (LFV) that can be induced by oceanic fronts. First, their slow changes in position and intensity can directly force similar changes in the atmospheric surface fronts they induce, and hence in the free atmosphere above. Second, the atmospheric response to a steady oceanic front might not be steady and thus generate LFV even when the oceanic forcing is constant. This second possibility has not been explored in previous LFV studies or even in studies of the mid-latitude coupled ocean–atmosphere system (Saravanan and McWilliams 1995; Neelin and Weng 1999; Weng and Neelin 1999; Gallego and Cessi 2001). This previous lack of attention to atmospheric LFV induced by fixed oceanic fronts is mainly due to the fact that, even in coupled general circulation model (GCM) studies, the grid size of the atmospheric GCM was typically 200–500 km, i.e. much larger than the cross-front scale of about 100 km.

Intraseasonal oscillations of 40–50 days were first observed in the tropical atmosphere by Madden and Julian (1971) and many studies of such oscillations since then have been reviewed by Madden and Julian (1994). Oscillations with both shorter and longer periods were described by Branstator (1987), Kushnir (1987), Dickey et al. (1991), Ghil and Mo (1991a, b), and Plaut and Vautard (1994) in mid-latitudes. A number of theoretical and modeling studies attribute the mid-latitude oscillations with periods of 15–40 days to the interaction of the jet stream with high mountain ranges such as the Rocky Mountains and the Himalayas (Jin and Ghil 1990; Ghil and Robertson 2000), while others attribute it to the barotropic instability of the zonally asymmetric climatological mean flow (Simmons et al. 1983). Lott et al. (2001) have provided strong observational evidence for the role of mountain torques in 15–30-day oscillations in the Northern Hemisphere. Plaut and Vautard (1994), on the other hand, found prominent 35- and 70-day oscillations over the Atlantic Ocean, where mountain torques are unlikely to play a major role.

In this study we examine the direct influence of long and narrow oceanic fronts, like the Gulf Stream in the Atlantic and the Kuroshio Extension in the Pacific, on the AMBL and the free atmosphere above it. In so doing, we find that these fronts can give rise to atmospheric LFV. The time scale that interests us is thus longer than a week, while previous studies concentrated on steady-state AMBL solutions (Hsu, 1987) or on the AMBL's short-time evolution (of the order of 12–24 hours).

An east–west oriented surface thermal front of finite zonal extent is shown in Fig. 1. The anticipated atmospheric circulation in its presence can be depicted as follows: Let us assume that the cold water lies to the north of the front. Thus the cold air also lies to the north and the warm air to the south of it. The wind near the sea surface blows therefore from north to south.

[**Fig. 1** near here, please.]

The maximum wind speed is obtained over the line segment of maximum thermal gradient, in the middle of the SST front, and decays towards its edges. Thus horizontal flow diverges north of the front and converges south of it. Consequently there is a downdraft north of the front and an updraft south of it. The resulting flow in a meridional plane perpendicular to the front spins up an eastward geostrophic jet. As this jet strengthens it becomes unstable. We study here the evolution of the entire atmospheric flow that is affected by the eastward jet and its instabilities.

In section 2 the atmospheric model is described. Section 3 deals with an approximate steady-state circulation, while in section 4 we study its instabilities, and the LFV so obtained. In section 5 we summarize and discuss these results.

2. The atmospheric model

The atmospheric model we use is composed of a steady, analytical AMBL and a time-dependent, numerical model for the free atmosphere above it. These two models are presented in the next two subsections.

2.1 The marine boundary layer (AMBL) model

The AMBL takes only several hours to adjust to the large-scale environmental conditions. This relaxation time is much shorter than the characteristic atmospheric and oceanic times, of weeks to years, in which we are interested here. We assume, therefore, that the AMBL is in instantaneous equilibrium with the oceanic front's SST field (Sweet et al. 1981), whether the latter itself is steady or slowly varying. In the present section 2.1 and throughout sections 3, 4.1 and 4.2, we take the SST anomaly field to be steady, $T = T(x, y)$, while in the section 4.3 it will be periodic, $T = T(x, y, t) = T(x, y, t+P)$, with period P longer than a year. Thus we shall take the perturbation Π in the AMBL's virtual potential temperature, at height $z = 0$, to equal T throughout this paper.

The pressure perturbation in the AMBL, at an arbitrary horizontal location (x, y), is thus found from the hydrostatic equation, combined with the equation of state:

$$\frac{1}{\rho_0}\frac{\partial p}{\partial z} = -\frac{g\rho}{\rho_0} = \frac{g\Pi}{\theta_0}. \qquad (1)$$

Integrating Eq. (1) from an arbitrary height z, within the AMBL, to its top H_E yields

$$\frac{p(z)}{\rho_0} = \frac{p(H_E)}{\rho_0} - \frac{g}{\rho_0}\int_z^{H_E}\rho(s)ds = \frac{p(H_E)}{\rho_0} - \frac{g}{\theta_0}(H_E - z)\Pi. \qquad (2)$$

Here ρ is the perturbation density, with ρ_0 its reference value and θ_0 that of Π, while g is the acceleration of gravity and f is the Coriolis parameter at a central latitude.

In the AMBL's frontal region the cold air from the north blows southward across the front, and results in a well-mixed AMBL. This yields an almost constant profile of the virtual potential temperature throughout the mixed layer, up to height H_E, with $\theta(z) - \theta(0) = T$, which justifies the approximation used for the integral in Eq. (2). The height H_E of the AMBL is given by $H_E = \pi(2k/f)^{1/2}$, where k is the turbulent eddy diffusion coefficient in the vertical direction (Holton, 1992), and $p(H_E)$ is the pressure

perturbation at the top of AMBL. We neglect herewith the difference in height between the top of the AMBL over the cold and the warm side of the front.

The horizontal gradient of the pressure perturbation is given by

$$\frac{1}{\rho_0}\frac{\partial p}{\partial x} = \frac{1}{\rho_0}\frac{\partial}{\partial x} p(H_E) - \frac{g}{\rho_0}(H_E - z)\frac{\partial \rho}{\partial x}, \qquad (3a)$$

$$\frac{1}{\rho_0}\frac{\partial p}{\partial y} = \frac{1}{\rho_0}\frac{\partial}{\partial y} p(H_E) - \frac{g}{\rho_0}(H_E - z)\frac{\partial \rho}{\partial y}. \qquad (3b)$$

The appropriate physical parameters are listed in Table 1. In this subsection, the variables are dimensional unless explicitly stated otherwise.

[**Table 1** near here, please.]

The pressure gradient in (3) has two components. One is due to the geostrophic wind in the free atmosphere at the top of the AMBL, that is

$$fv_G = \frac{1}{\rho_0}\frac{\partial p(H_E)}{\partial x}, \; fu_G = -\frac{1}{\rho_0}\frac{\partial p(H_E)}{\partial y},$$

and is independent of z. The second one is due to the thermal oceanic front and it is a function of z.

The linear equations of motion in the AMBL are:

$$k\frac{\partial^2 u}{\partial z^2} + fv - \frac{1}{\rho_0}\frac{\partial p}{\partial x} = 0, \qquad (4a)$$

$$k\frac{\partial^2 v}{\partial z^2} - fu - \frac{1}{\rho_0}\frac{\partial p}{\partial y} = 0. \qquad (4b)$$

The boundary conditions are:

$$u = v = 0 \text{ at } z = 0, \qquad (5a)$$

$$u = u_G, \; v = v_G \text{ as } z \to \infty \; . \qquad (5b)$$

At the top of the AMBL we also need a condition that assures the continuity of the momentum flux at $z = H_E$, since $\frac{\partial}{\partial z}\left(k\frac{\partial p}{\partial x}\right)$, $\frac{\partial p}{\partial y}$ in Eqs. (3a,b) is discontinuous at H_E. The appropriate conditions are:

$$u_{-} = u_{+},\ v_{-} = v_{+},\ k\frac{\partial u}{\partial z_{-}} = k\frac{\partial u}{\partial z_{+}},\ k\frac{\partial v}{\partial z_{-}} = k\frac{\partial v}{\partial z_{+}}, \tag{6}$$

where the subscripts + and – stand for the limits from above and below $z = H_E$.

The closed-form, analytical solution to Eq. (4) in the AMBL, using Eq. (3), the boundary and continuity conditions (5) and (6), and geostrophic balance in the free atmosphere, is:

$$\begin{aligned} u(z) = u_G + \frac{g}{f\rho_0}(H_E - z)\frac{\partial T}{\partial y} &- e^{-\zeta z/H_E}\left[u_G\cos(\zeta z/H_E) + v_G\sin(\zeta z/H_E)\right] \\ &+ e^{-\zeta z/H_E}\frac{g}{f\rho_0}H_E\left(\frac{\partial T}{\partial x}\sin(\zeta z/H_E) - \frac{\partial T}{\partial y}\cos(\zeta z/H_E)\right) \\ &+ \frac{g}{f\rho_0}\frac{H_E}{4\zeta e^{\zeta}}\left(e^{\zeta z/H_E} - e^{-\zeta z/H_E}\right)\left(\frac{\partial T}{\partial x} - \frac{\partial T}{\partial y}\right)\cos(\zeta z/H_E) - \left(e^{\zeta z/H_E} + e^{-\zeta z/H_E}\right)\left(\frac{\partial T}{\partial x} + \frac{\partial T}{\partial y}\right)\sin(\zeta z/H_E), \end{aligned} \tag{7a}$$

$$\begin{aligned} v(z) = v_G - \frac{g}{f\rho_0}(H_E - z)\frac{\partial T}{\partial x} &+ e^{-\zeta z/H_E}\left[u_G\sin(\zeta z/H_E) - v_G\cos(\zeta z/H_E)\right] \\ &+ e^{-\zeta z/H_E}\frac{g}{f\rho_0}H_E\left(\frac{\partial T}{\partial x}\cos(\zeta z/H_E) + \frac{\partial T}{\partial y}\sin(\zeta z/H_E)\right) \\ &+ \frac{g}{f\rho_0}\frac{H_E}{4\zeta e^{\zeta}}\left(e^{\zeta z/H_E} - e^{-\zeta z/H_E}\right)\left(\frac{\partial T}{\partial x} + \frac{\partial T}{\partial y}\right)\cos(\zeta z/H_E) + \left(e^{\zeta z/H_E} + e^{-\zeta z/H_E}\right)\left(\frac{\partial T}{\partial x} - \frac{\partial T}{\partial y}\right)\sin(\zeta z/H_E), \end{aligned} \tag{7b}$$

where we have assumed that $\Gamma(x, y, z, t) = T(x, y)$.

Given u and v throughout the AMBL, we obtain the vertical velocity at its top by integrating the continuity equation:

$$w(H_E) = -\int_0^{H_E}\left(\frac{\partial u}{\partial x} + \frac{\partial v}{\partial y}\right)dz = \zeta_G\frac{H_E}{2\zeta}(1 + e^{-\zeta}) - \frac{gH_E^{\,2}}{2\zeta f\rho_0}\nabla^2 T\left(\frac{1}{2\zeta} + e^{-\zeta}\left(1 - \frac{1}{\zeta}\right) - \frac{e^{-\zeta}}{2\zeta}\right) \tag{8}$$

here

$$\zeta_G \equiv \frac{\partial v_G}{\partial x} - \frac{\partial u_G}{\partial y}$$

is the vorticity of the geostrophic wind at $z = H_E$, and $\nabla^2 T \equiv \left(\partial^2/\partial x^2 + \partial^2/\partial y^2\right)T$ is the Laplacian of the SST field. Thus the vertical velocity at the top of the AMBL can be approximated by:

$$w(H_E) = \frac{H_E}{2}\zeta_G - \frac{gH_E}{f_0}\left(1 - \frac{1}{2}\right)^2 T. \tag{9}$$

It has two components, one due to the geostrophic flow above the AMBL, the other due to the wind induced in the AMBL by the oceanic thermal front.

2.2 The QG model in the free atmosphere

In the free atmosphere above the AMBL we use a quasi-geostrophic (QG) model with a single, equivalent-barotropic mode in the vertical. This mode is described by the streamfunction $\psi = \psi(x, y, t)$. The model equations are nondimensionalized by the following characteristic scales:

$$X, Y \quad L; \qquad Z \quad H; \qquad T_i \quad L/V; \quad \psi \quad VL. \tag{10}$$

Here L is the horizontal length scale across the front, H is the vertical scale of the free atmosphere, T_i is the time scale, and V scales the wind speed in the cross-front direction. The appropriate scales are listed in Table 1, along with the main physical parameters. In this subsection, a star indicates the dimensional variables.

The nondimensional potential vorticity (PV) equation with this scaling is

$$\frac{\partial q}{\partial t} + \beta\frac{\partial \psi}{\partial x} + J(\psi, q) = r_H \nabla^4 \psi + \frac{\partial w_a}{\partial z}, \tag{11}$$

where w_a is the vertical velocity in the free atmosphere (Pedlosky 1987; Holton 1992). The relative PV is given by

$$q \equiv \nabla^2 \psi - \gamma^2 \psi \tag{12}$$

and the nondimensional parameters β, γ and r_H by

$$\beta = \beta_0 \frac{L^2}{V}, \quad \gamma = \frac{L}{R_d}, \quad r_H = \frac{E_H}{2} = \frac{A_H}{VL}; \tag{13}$$

β_0 is the meridional gradient of f, R_d is the Rossby radius of deformation of the atmosphere, A_H is the dimensional horizontal diffusion coefficient, $\varepsilon = V/fL$ is the Rossby number, based on the cross-frontal

speed V, and $E_H = 2A_H/fL^2$ is the horizontal Ekman number. We shall also use later the Froude number $Fr = V(gH_E)^{-1/2}$.

Integrating Eq. (11) with respect to z from $z = 0$ to $z = H_a/H$, the (nondimensional) height of the free atmosphere (see Table 1), and dividing by this height H_a/H, we obtain:

$$\frac{\partial q}{\partial t} + \beta\frac{\partial \psi}{\partial x} + J(\psi, q) = r_H\nabla^4\psi - \frac{H}{H_a}w_a(x, y, z = 0, t). \tag{14}$$

The lower boundary condition for the free atmosphere is:

$$\frac{H}{H_a}w_a(x, y, z = 0,\ t) = \frac{1}{\beta}\frac{L}{H_a}\frac{w^*}{V} = \frac{\gamma}{\beta_0}\nabla^2 T^* + \beta\frac{L}{V}\beta^*. \tag{15}$$

According to the usual conventions of boundary-layer theory (Batchelor 2000), $z = 0$ here is understood to apply at the top of the AMBL. Thus w^*, T^* and β^* in (15) are the dimensional values of the vertical velocity given by Eq. (9), the SST, and the geostrophic vorticity at the top of the AMBL. Along the meridional boundaries $\psi = q = 0$, while in the zonal direction we use periodic boundary conditions in ψ and q.

The nondimensional constant

$$\alpha = \left(1 - \frac{1}{2\beta}\frac{gH_E}{H_aV^2}\frac{k}{2f}\right)^{1/2} = \frac{1}{2\beta}\left(1 - \frac{1}{2\beta}\frac{gH_E^2}{H_aV^2}\right) = \frac{1}{2\beta}\left(1 - \frac{1}{2\beta}\frac{H_E}{H_a}\frac{1}{Fr^2}\right) \tag{16}$$

determines the strength of the vertical velocity component at the top of the AMBL that is induced by the oceanic thermal front. It is proportional to the inverse square Froude number of the AMBL. The nondimensional constant

$$\gamma = \frac{1}{2\beta}\frac{H_E}{H_a}\frac{fL}{V} = \frac{1}{2\beta}\frac{H_E}{H_a} \tag{17}$$

determines the strength of the vertical velocity component at the top of the AMBL that is due to the geostrophic wind. It is proportional to the inverse of the frontal Rossby number. We see that $\Box \sim 1/Fr^2$, $\Box \sim 1/\Box$, and both are proportional to H_E/H_a.

The numerical scheme is the same as in Feliks (1990) and in Feliks and Ghil (1996). Key features include fourth-order accurate discretization by finite elements in the horizontal (cf. Haidvogel et al. 1980), a second-order Adams-Bashforth scheme in time, and use of a fourth-order Shapiro (1970) filter at every time step.

3. Steady-state solutions

3.1 The AMBL steady state

First we analyze the steady flow induced in the AMBL by an east–west oceanic front that extends to infinity in the $\pm x$ directions. We prescribe the following meridional, x-independent structure for the latter:

$$T = \Box T_a \tanh(y/d), \tag{18}$$

where d is the cross-frontal scale and T_a is the strength of the front. For this temperature profile, the difference in SST between the two water masses separated by the front is $2T_a$, the width of the front is roughly $4d$, and all the fields in the solution are also independent of x.

Since the AMBL model is linear, the wind speed is proportional to T_a; see Eq. (7). Thus we examine below the case where $T_a = 1$ °C and $d = 50$ km, while $k = 3.3$ m^{2}s^{-1}. We show in Fig. 2a a cross-section of the SST as a function of y; that part of the vertical velocity w at the top of the AMBL that is induced by the SST field is shown in Fig. 2b. In this case, the SST-induced w has its maxima of ± 0.9 cms^{-1} about 30 km off the axis of the front, to the north and south, respectively, where $\partial^2 T/\partial y^2$ has its maximum; see Eq. (9).

[**Fig. 2** near here, please.]

In Fig. 3, the vertical profiles of u and v at $y = 0$ are shown. The maximum of u is at 325 m and that of v is at 200 m. The vertical profiles of u and v at other points are the same but the amplitude is smaller since $\partial T/\partial y$ has its maximum at $y = 0$.

[**Fig. 3** near here, please.]

The AMBL model used here is linear, i.e. the nonlinear advection terms are omitted in the momentum equation (4). This assumption is examined below for a weak front, $T_a = 1$ °C, which corresponds to a temperature gradient of (2 °C)/(200 km), as well as for a strong front, $T_a = 3.5$ °C, which corresponds to a temperature gradient of (7 °C)/(200 km). The latter value of the temperature gradient equals approximately the one found across the Gulf Stream and Kuroshio fronts.

We examine in Fig. 4 the different terms in Eq. (4b) vs. the nonlinear advection term $v\partial v/\partial y$, which was omitted from the equation. The nonlinear term is crudely estimated here from the linear solution (7).

[**Fig. 4** near here, please.]

This estimate reaches its maximum at $z = 200$ m and $y = \pm 30$ km. For weak fronts, $T_a = 1$ °C, the nonlinear advection term is several times smaller than all the other terms (see Figs. 4a,c) and so it can safely be neglected. For strong fronts, $T_a = 3.5$ °C, the nonlinear term is not small at altitudes around 200 m, provided $|y| > 20$ km (see Fig. 4d). It is then comparable to the Coriolis and dissipation terms and to half the pressure term. At lower altitudes, $z < 120$ m, though, the balance is mainly between the pressure and diffusion terms, and the nonlinear term is significantly smaller (see Fig. 4b). At higher altitudes, $z >$ 300 m, the main balance is geostrophic, between the pressure and Coriolis terms, and the nonlinear term is again significantly smaller (see Fig. 4b). It is only at intermediate heights, where Ekman balance between all three linear terms prevails, and for strong fronts that the nonlinear term is no longer negligible.

There are thus parts of the AMBL where, in the case of strong fronts, the cross-frontal advection term becomes comparable with the smaller one(s) among the linear terms. Still, for an exploratory study like the present one, the linear approximation in the AMBL model seems fairly well justified.

3.2 The steady flow in the free atmosphere

We now let the vertical velocity $w = w(H_E)$ induced by the infinite oceanic front (18) at the top of the boundary layer spin up the circulation in the free atmosphere above the AMBL; the dynamics of the latter is governed by the equivalent-barotropic QG model of section 2.2. A steady-state flow can be obtained in the free atmosphere when the vertical velocity component induced by the oceanic front is exactly balanced by the opposite vertical velocity component induced by the geostrophic wind at the top of the AMBL.

Using the approximate Eq. (9) yields the following balance, when setting $w(H_E) = 0$:

$$\Box_G^* = \left(1 \Box \frac{1}{2\Box}\right)\left(\frac{gH_E}{f\Box_0}\right)\left(\frac{\partial^2 T^*}{\partial x^{*2}} + \frac{\partial^2 T^*}{\partial y^{*2}}\right); \tag{19}$$

asterisks here indicate dimensional quantities. By integrating the above equation with respect to y, from $y = -$ to y^*, we obtain the explicit form for the geostrophic wind at height H_E and meridional position y^*:

$$u_G^*(y^*, H_E) = \left(1 \Box \frac{1}{2\Box}\right)\left(\frac{gH_E}{f\Box_0}\right)\frac{\partial T^*}{\partial y^*}(y^*) \Box \frac{\partial T^*}{\partial y^*}(\Box) = \left(1 \Box \frac{1}{2\Box}\right)\left(\frac{gH_E}{f\Box_0}\right)\frac{\partial T^*(y^*)}{\partial y^*}$$

$$= \left(1 \Box \frac{1}{2\Box}\right)\left(\frac{gH_E T_a}{f\Box_0}\right)\frac{\operatorname{sech}\left(y^*/d\right)^2}{d}. \tag{20}$$

The geostrophic flow at the top of the AMBL is thus proportional to the oceanic front's strength T_a and to the AMBL height H_E, while it is inversely proportional to the frontal width d. The geostrophic velocity $u_G^* = u_G^*(y^*, H_E)$ is shown in Fig. 5 for a weak front, T_a = 1 °C. The flow is

parallel to the frontal isotherms. The maximum zonal velocity is obtained at $y = 0$ and it equals 4.43 ms^{-1}.

[**Fig. 5** near here, please.]

Such a symmetric eastward jet profile is called a Bickley jet (Kuo 1973; Haltiner and Williams 1979, Sec. 4.4) and it has two inflection points. The necessary condition for it to experience barotropic instability, in the absence of lateral viscosity and bottom friction, is $-2 < \beta d^2 / U_0 < 2/3$, where U_0 is the maximal velocity. In our case $U_0 = u_G(y^* = 0, H_E) = (1 - 1/2\sigma) g H_E T_a / f d \beta_0$ and thus, for $d = 50$ km, it is necessary for U_0 to exceed 0.07 ms^{-1} in order for such a jet to be unstable. To reach this threshold requires, therewith, a much smaller value of T_a than the one that corresponds to the Gulf Stream and Kuroshio fronts, at least in the present, unrealistic case of an infinite oceanic front, without lateral-viscosity effects. We consider both lateral-viscosity and finite-length effects in the next section.

4. Time-dependent solutions

4.1 Finite-length effects

The case of an infinite oceanic front was treated in section 3.2 analytically, for orientation purposes. In fact, we are more interested in the case, illustrated in Fig. 1, of an oceanic thermal front of finite length. This case represents a better approximation of the thermal fronts associated with the Gulf Stream and the Kuroshio Extension and it will have to be treated numerically. For such an oceanic front, the steady-state solutions differ significantly from the idealized ones given in the previous section, and so does their stability. In the next subsection, we carry out a systematic study of the dependence of the finite-front solutions and of their stability on the frontal strength T_a.

To motivate this study, we examine in the present subsection a strong thermal front that shares certain characteristics with the Gulf Stream and Kuroshio fronts. The length of the front is $L_x = 600$ km, its strength is $T_a = 3.5$ °C, and its width is $d = 50$ km. These values give a temperature change of roughly

(7 °C)/(200 km), for the hyperbolic-tangent profile of Eq. (18). The other parameters are listed in Table 1. The computational domain size is 4000 km x 3500 km, with a grid size of $\Delta x = \Delta y = 50$ km, and a time step of $\Delta t = 800$ s. The corresponding nondimensional values we actually use are divided by L for length and T_i for time.

Due to computational limitations we cannot study the model dynamics as a continuous function of the external parameters while using a sufficiently small grid size to describe accurately the Laplacian $\nabla^2 T$ of the oceanic thermal front's SST field. To capture, with satisfactory accuracy, the influence of the oceanic front on the evolution of our atmospheric model at the resolution of 50 km, we adjust the strength T_a of the oceanic front, replacing it by $T_* = AT_a$.

We determine the correction factor A so that the vorticity pumped by the AMBL into the free atmosphere on the "coarse" grid will be the same as in the analytical solution. The vertical velocity within the first grid cell away from the front is the most important since, for a frontal width of $d = 50$ km, the maximum vertical velocity is obtained at $y = \pm 30$ km (see Fig. 2b). To find the correction factor A, we average the analytical vertical velocity w_a in Eq. (15) over a grid cell and compare it with the numerical average of w_a, i.e.:

$$A = \left[\frac{T(y - \Delta y) - 2T(y) + T(y + \Delta y)}{\Delta y^2} \right] \Delta y \left[\int_{y-\Delta y}^{y+\Delta y} \frac{\partial^2 T}{\partial y^2} dy \right]^{-1}. \qquad (21)$$

The result for the front of interest to us is $A = 2.06$; for example $T_a = 3.5$ °C is thus corrected to $T_* = 7$ °C on the grid we use. In the absence of this correction, that is for $A = 1$, the atmospheric response to a strong oceanic front is quite weak when using $\Delta x = \Delta y = 50$ km.

The oceanic front shown in Fig. 1 corresponds to the choice of $T_* = 7$ °C and $d = 50$ km. It has the following spatial pattern:

$$T(x, y) = -T_a \tanh[y/a(x)]; \qquad (22a)$$

here

$$a(x) = \begin{cases} D, & x \le x_0, \\ d + \dfrac{x - x_1}{x_0 - x_1}(D - d), & x_0 \le x \le x_1, \\ d, & x_1 \le x \le x_2, \\ d + \dfrac{x - x_2}{x_3 - x_2}(D - d), & x_2 \le x \le x_3, \\ D, & x_3 \le x, \end{cases} \qquad (22b)$$

while d = 50 km, D = 2000 km, x_0 = 400 km, x_1 = 600 km, x_2 = 1200 km, and x_3 = 1400 km.

The spin-up process begins from a free atmosphere at rest. An atmospheric jet forms above the oceanic front and two gyres form to either side of this jet: cyclonic to the north and anticyclonic to the south (see Fig. 6, snapshot at t = 8 nondimensional units). At this early stage in the spin-up, the jet terminates fairly abruptly, at $x \approx 2000$ km, with a zone of diffluence where it splits into the return flows of the two gyres. Subsequently, the jet and the gyres spread eastward due to advection of the momentum by the jet itself (see t = 24 and t = 216 in the figure). The length of the atmospheric jet is now almost 3000 km, more than four times the length of the oceanic front (see t = 216 and 224). For orientation, T_i = 0.58 days (see again Table 1), so that t = 10, 100, 1000 in nondimensional time units corresponds roughly to 6, 60, and 600 days.

[**Fig. 6** near here, please.]

The growth of the jet's penetration length, and of the zonal extent of the recirculation gyres, as apparent in the first three panels of Fig. 6, is observed in all the other numerical simulations we carried out. It will be explained in section 5.

The jet reaches a maximum zonal speed of 9 ms^{-1} at t = 216, mainly near the eastern end of the oceanic front. This speed is about 60% of that predicted by the analytical solution for a steady-state jet and an infinite oceanic front; see Eq. (20). This difference is mainly due to momentum advection eastward by the jet itself to regions that are not influenced directly by the intense segment of the oceanic

front. So the vorticity and energy pumped through the AMBL over the finite oceanic front region is mainly balanced by this advection, and not by bottom friction, as in Eq. (9), from which (20) was obtained.

At $t = 224$, the zonal jet in the free atmosphere becomes unstable and its eastern end starts to meander. This barotropic instability is due to the jet's strong horizontal shear. The most unstable wave has a length of about 500 km. The process of energy transfer from the AMBL that overlies the oceanic front to the jet, and from the jet to the large-scale gyres, continues to maintain the large-scale circulation, nonobstant this instability. The energy flux from the jet to the gyres is balanced by friction with the sea surface, through the AMBL, which extracts energy from the gyres at its top.

At later times, eddies detach from the meanders along the downstream, eastern portion of the jet; see for instance the panels at $t = 3968$–3992 in Fig. 6. The detached anticyclonic eddies move northward along the eastern tip of the cyclonic gyre, while the cyclonic eddies move southward along the eastern tip of the anticyclonic gyre. These eddies do not seem to penetrate the large gyres themselves, which would eventually weaken their vorticity; instead, they are themselves weakened and washed downstream.

The model was run at $T_* = 7$ °C for $t = 10$ years (i.e., 6293 nondimensional time units) and showed every sign of entering into a statistically stationary regime. We discarded the first 4 years, so as to eliminate any transients, and examined only the time series of the last 6 years. In this stationary regime, the solution is aperiodic in time and asymmetric in space. The streamfunction and PV fields were saved every 500 time steps, i.e., every 4.63 days.

In order to extract coherent spatio-temporal structures from the streamfunction field, we performed multichannel singular-spectrum analysis (M-SSA; see Plaut and Vautard 1994; Ghil et al. 2002). To keep the size of the covariance matrices that need to be diagonalized manageable, we used

only every second grid point along each axis; that is, 40 x 35 grid points were used in obtaining the spatial empirical orthogonal functions (EOFs). In the M-SSA, we retained the ten leading principal components (PCs) of the spatial analysis, which capture 94.6% of the total variance.

The first two eigenmodes in the M-SSA capture, in turn, 26% of this leading spatial variance, that is, 24.6% of the total variance; these two modes have a dimensional period of 68 days. The window width was equal to 30 sampling intervals, that is about 139 days. The fields used in all the time series analysis correspond to averages over each sampling interval; the instantaneous snapshots at these intervals are the ones plotted when discussing the raw data (such as in Fig. 6).

The power spectrum of the mean kinetic energy, defined over a subdomain that encompasses the most intense portion of the jet, is shown in Fig. 7a. It was calculated by the classical Blackman-Tukey lag-correlation method, with 128 lags, and shows a dominant peak at 66–72 days, accompanied by a much smaller peak at 34–38 days. When using other scalar time series extracted from the solution, the 68-day peak is still prominent (not shown).

[**Fig. 7** near here, please.]

Eight equally spaced phases of the 68-day oscillation, reconstructed with the two leading M-SSA modes, are shown in Fig. 7b; the compositing of these 8 phases follows the methodology of Moron et al. (1998; see their appendix). The mean of the streamfunction field over the last 6 years of the simulation for $T_* = 7$ °C is shown in Fig. 8d.

[**Fig. 8** near here, please.]

A positive anomaly begins to develop in the diffluent portion of the jet, near its axis, in phases 4 and 5 of Fig. 7b. This anomaly grows in place and expands in phases 6 and 7, blocking the antisymmetric flow. The positive anomaly then decays and a negative anomaly begins to develop through phases 8 and 1. The extremum of either anomaly, positive or negative, propagates very slowly

eastward. This propagation is due to advection by the jet itself, and is thus a nonlinear property of the finite-amplitude, saturated oscillation, while the initial development of the anomaly is due to linear barotropic instability of the jet's meridional shear.

We examined the influence of the horizontal resolution on the solution by taking $\Delta x = \Delta y = 25$ km, that is the number of grid points was increased by a factor of 4, from about 5600 points to roughly 22400. In this case the correction factor A given by Eq. (21) is very close to 1.0, $A = 1.3$. The general behavior and characteristics of the solution, e.g. the peaks in its power spectrum, are very similar to those obtained with the grid size of 50 km (not shown). We conclude that the relatively coarse grid of 50 km is entirely adequate for this study, given a suitably corrected frontal forcing.

4.2 The LFV's dependence on the oceanic forcing's intensity

We now study the model dynamics as a function of the corrected frontal strength T_*, keeping the frontal width $d = 50$ km fixed in Eq. (22). For $T_* \leq 4$ °C the solution in the free atmosphere is steady and exhibits two large, antisymmetric gyres — cyclonic in the domain's northern part and anticyclonic in its southern part — separated by a purely zonal jet (Fig. 8a). Note that this result is quite distinct from the one that would be obtained for an infinite oceanic front, where the streamlines in the free atmosphere would still be parallel to the oceanic isotherms and there would be no recirculation. As discussed at the end of section 3.2, the Bickley jet so obtained would be barotropically unstable for such values of T_*.

For 4 °C $< T_* <$ 5 °C the solution becomes periodic in time and asymmetric in space, with a period of 31 days. For $T_* = 4.5$ °C, the mean with respect to time of the streamfunction is still antisymmetric and shown in Fig. 8b. This mean is very similar to the steady solution that obtains for $T_* \leq 4$ °C (Fig. 8a) but it exhibits a slightly more intense circulation.

The anomaly of these periodic solutions, i.e. the difference between the instantaneous streamfunction and its time mean, can be decomposed into an antisymmetric and a symmetric

component. The antisymmetric component is smaller by an order of magnitude than the symmetric one and plays no significant role in the dynamics for values of the forcing T_* that are close to the onset of the oscillatory instability. The symmetric component is shown in Fig. 9 for a half cycle of the flow field's evolution over the period of 31 days, at T_*= 4.5 °C.

[**Fig. 9** near here, please.]

This dominance of the symmetric component (see Figs. 7b and 9) is in good qualitative agreement with the rigorous mathematical results of Chen et al. (2002). These authors studied the full partial differential equations governing a forced, dissipative QG jet on a β-plane in an x-periodic channel, subject to zonal forcing with a meridionally antisymmetric profile, and showed that Hopf bifurcation occurs through a spatio-temporal mode that has a spatially symmetric pattern and a frequency that is lower than that of the problem's free Rossby waves (i.e., in the absence of forcing and dissipation).

A rough calculation of Rossby wave propagation on a Bickley jet (cf. Kuo 1973; Haltiner and Williams 1979, section 4.4) gives periods of the order of several days. These are, indeed, clearly shorter than the 68 days we find for the oscillatory instability here.

The anomalies of the symmetric mode at t = 3960 have almost exactly the same pattern and the opposite sign when compared to those at t = 3984. This mode has a wave pattern of about 1500 km in length, which propagates eastward due to advection by the jet. The cellular features of this mode strengthen as they move eastward, until they reach the diffluence region of the jet, at $x \sqcup 60$. As the cells continue to propagate further eastward they start to weaken. The intensification of the cells occurs probably by extracting energy from the mean jet over the portion where it is strongest. The subsequent weakening occurs as dissipation is no longer exceeded by the local forcing.

For $T_* \geq 5$ °C the solution becomes chaotic. At $T_* = 5$ °C the dominant peak in the solution's power spectra has a period of 26 days (not shown). Increasing the oceanic front's intensity further to $T_* = 6$ °C, the dominant peak shifts fairly suddenly to a period of 74 days. The time mean of the streamfunction in Fig. 8c is still antisymmetric and resembles the steady solution of Fig. 8a.

The symmetric and antisymmetric components of the dominant oscillatory mode are shown in Fig. 10 at two different epochs, 37 days apart, for $T_* = 6$ °C. At this value of T_* the 74-day mode is quite apparent as nearly periodic spells and the plots in the figure were obtained by sampling these oscillatory spells. The symmetric mode has almost the same pattern, with opposite sign, at these two times (Fig. 10, left panels). The meridional scale of the anomaly is about 1000 km and the zonal scale is about 2000 km. The amplitude of the antisymmetric mode (Fig. 10, right panels) is about 1/3 of the amplitude of the symmetric mode, i.e. the relative importance of the former tends to grow with T_*.

[**Fig. 10** near here, please.]

The case in which the intensity of the oceanic front is even larger, $T_* = 7$ °C, was already studied in the previous subsection. The time mean of the streamfunction is still antisymmetric, as seen in Fig. 8d. The spatial extent of significant anomalies in this case is greater: the symmetric mode is still dominant and it covers an area of about 2000 km x 2000 km, as shown in Fig. 7b.

From the above solutions we can conclude that, as the oceanic front becomes more intense, the prominent periods in the power spectrum increase. This increase is not monotonic: for $T_* = 4.5$ °C the period is 31 days, while for $T_* = 5$ °C it is 26 days, but for $T_* = 6$ °C the period is 74 days, and for $T_* = 7$ °C it is 65 days (see section 3.2). Overall, the instabilities with longer periods have also a spatially larger extent, although the physical mechanism of the instability appears to be the same. The spatially larger extent implies the need to extract more energy from the oceanic front. Since the dissipation is linear, the

longer period might be a result of the longer time required for the equilibration of the energy fluxes into and out of the free atmosphere, across the top of the AMBL.

4.3 The influence of slow changes in the SST front on the atmospheric LFV

In the following experiment we explore the influence of ultra-low-frequency changes on the model atmosphere's LFV. Interannual and interdecadal variability in mid-latitude SSTs are known to occur in the North Atlantic and North Pacific (Bjerknes 1964; Deser and Blackmon 1993; Kushnir 1994; Speich et al. 1995; Moron et al. 1998; Chao et al. 2001).

In this experiment the spatial structure of the oceanic front is the same as in Fig. 1; see also Eqs. (22a,b) in section 4.1. In the previous experiments, T_a in Eq. (22*a*), and hence the corrected value $T_* = AT_a$, was constant in time. In the present experiment we allow T_* to be time dependent:

$$T_*(t) = 6 + \sin(\Pi t), \qquad (23)$$

where $\Pi = 2\pi/7$ yr^{-1}, i.e. the perturbation in the frontal strength has a period of 7 years and an amplitude of 1 °C.

The time series of the solution's kinetic energy is shown in Fig. 11a. Two distinct regimes can be identified: a high-energy regime with large fluctuations and a low-energy regime with small fluctuations. In the high-energy regime, the flow in the free atmosphere (Fig. 11b, t = 5834) is characterized by a strong zonal jet and vigorous eddies that detach from it, as in Fig. 6. In the low-energy regime (Fig. 11b, t = 3153), the eddies are weaker and the jet meanders but slightly. The intervals of high and low energy overlap the intervals during which the SST front, and hence $\left|\nabla^2 T\right|$, are strong and weak, respectively. The atmospheric jet's intensity is determined by the injection of vorticity into the free atmosphere, and this injection is proportional to $\left|\nabla^2 T\right|$; see Eqs. (14) and (15).

[**Fig. 11** near here, please.]

The model was run with the periodic forcing (23) for 50 years and only the last 46 years where analyzed. To describe the spatio-temporal features of the model response, we used again the M-SSA method, as in section 4.1. Since we are interested here in periods of several years, the periods of less than three months were filtered out by calculating the moving average over this window. After this prefiltering, the ten leading EOFs of the spatial PC analysis capture 99.5% of the variance. They were analyzed using a window width of 80 times the 3-month sampling interval, that is of 20 years.

The only oscillation found to be statistically significant has a period of 7 years and is captured by eigenmodes (1,2) in the M-SSA analysis. The 8 phases of the reconstructed oscillation are plotted in Fig. 12. The figure clearly shows a standing, purely forced oscillation.

[**Fig. 12** near here, please.]

The mean of the streamfunction over the last 46 years (not shown) is quite similar to that obtained for a time-constant forcing with $T_* = 6$ °C (see again Fig. 8c). The anomalies in Fig. 12 are mainly antisymmetric and of one sign on either side of the domain's symmetry axis; the only noteworthy exception occurs as a dipole of variable extent and intensity in the zonal jet's diffluent region. When the anomalous flow is predominantly cyclonic to the north and anticyclonic to the south of the symmetry axis, the anomaly strengthens the mean flow; the opposite is the case when the anomaly has the opposite vorticity. The dipole in the jet's diffluent region grows and decays in extent and intensity in phase with the intensity of the dominant anomaly, while each of its two poles has a vorticity that is opposite in sign to that of the adjacent gyre anomaly. Hence during high-energy intervals the jet is shorter than during the low-energy intervals.

We next examine the atmospheric LFV in the high- and low-energy regimes. In the low-energy regime the dominant period is about 33 days, while in the high-energy regime it is about 70 days. The time–frequency diagram of the streamfunction was computed using a short-time Fourier transform, at a

point where the LFV is most prominent, and is shown in Fig. 13a; this point is the grid point (45, 0), situated along the jet axis, close to the point of diffluence. The periods of 70–100 days are absent or weak during the low-energy intervals (e.g., years 4–6 and 11–13), while the 25–40-day activity is missing during high-energy intervals (years 7–11 and 13–16). The higher-frequency activity is less pronounced, even when it is strongest, as seen from the time series itself (Fig. 13b).

[**Fig. 13** near here, please.]

The spatio-temporal structure of the 33- and 70-day oscillation was reconstructed using M-SSA (not shown). The anomalies are mainly symmetric with respect to $y = 0$ in both cases. The 33-day oscillation in this periodically forced case is very similar to the 30-day oscillation shown in Fig. 9 for the case $T_* = 45$ °C. Likewise, the 70-day oscillation in the present case is very similar to the 68-day oscillation shown in Fig. 7b for the case $T_* = 7$ °C.

Since the externally imposed period of 7 years is so much longer than the internal periods of about 30 and 70 days, the present results are not surprising. When the front is weak, the 30-day oscillation dominates, as it does for time-constant weak forcing. When the front is strong, the 70-day oscillation is dominant, as it is for time-constant strong forcing. The situation is thus similar to that found by Strong et al. (1993, 1995) in a QG, barotropic model on the sphere. The model had an intrinsic period of 40 days for Northern Hemisphere winter conditions and one of 15 days for summer conditions. When the forcing was allowed to vary seasonally, the results were essentially the same. It is only when the external and internal periods are closer to each other that interesting nonlinear interactions are expected to arise (Jin et al. 1994, 1996; Tziperman et al. 1994).

5. Concluding remarks

5.1 Analytical boundary layer model

In this paper we studied the atmospheric flow induced by an oceanic front. The atmosphere was modeled by coupling a very simple, linear model of the marine boundary layer (AMBL) to a quasi-geostrophic (QG), equivalent-barotropic nonlinear model of the free atmosphere, driven by the flow in the AMBL. A simple analytical formulation was found for the vertical velocity at the top of AMBL. The vertical velocity induced by the oceanic front is proportional to the Laplacian of the sea surface temperature (SST) field.

We obtained an analytical solution for the flow in the free atmosphere when imposing an oceanic front of infinite length (Figs. 2 and 3). This solution was found to justify the neglect of nonlinear terms in the AMBL model (Fig. 4).

5.2 Penetration length of the atmospheric jet

We examined next the spin-up of the flow in the free atmosphere, when driven by an oceanic thermal front of 600 km in length and a thermal gradient of (3.5 °C)/(100 km) (see Fig. 1). The evolution of the flow in this numerical simulation helped motivate the subsequent, detailed investigation of the atmospheric flow's dependence on the intensity of the oceanic front. A jet with two large gyres, cyclonic to the north and anticyclonic to the south, spins up from rest over the oceanic front (Fig. 6). At first, the jet is flowing eastward, parallel to the frontal isotherms. This jet strengthens, lengthens and becomes unstable as the spin-up progresses. The most unstable wave has a wavelength of about 500 km. This wave grows to form a large meander and later eddies detach from the downstream end of the jet. These eddies propagate around the eastern tip of the gyres.

The zonal extent of the atmospheric jet grows during the spin-up from hardly more that the 600 km where the finite-length oceanic front is most intense to several times that length. This growth is

found to occur in all our numerical simulations (Figs. 6, 8, and 11b, c). In all these simulations, a limiting value L_x^o of the jet's zonal extent is found; the length L_x^o is defined as the distance along the *x*-axis between the point where the maximum speed $U_{\max}$ is attained and the point downstream where the speed falls off to $U_{\max}/e$.

The existence of such a limit to the length of zonal jets follows from the theory of geostrophic turbulence (Charney 1971) in the presence of the β-effect (Rhines 1975). Salmon (1998, section 6.3) describes, in particular, the effect of localized mid-latitude stirring of an initially quiescent flow in a periodic β-channel. In our case, the localized stirring is provided by the finite-length, east–west oriented front, which induces no net momentum into the atmosphere. The resulting flow is, as predicted by the considerations of potential eustrophy conservation, strongly eastward near the latitude of the stirring and weakly westward everywhere else; see Eq. (3.19) and Fig. 6.4 in Salmon (1998).

The theoretical value of the eastward jet's maximal extent is given by a comparison of the eddy-turnover time with the Rossby-wave period. This comparison results in the definition of the Rhines scale $k_\beta \equiv (\beta/\overline{U})^{1/2}$, where $\overline{U}$ is the root-mean-square velocity of the flow and a wave vector $\mathbf{k} = (k_x, k_y)$ has length k. The scale k_β separates the domain in wave number space where the energy cascade to lower wave numbers (that is, longer scales) is effective from that where it is not.

Theoretically, the jet's penetration length in our β-channel is limited by the smallest k_x that satisfies

$$\frac{\beta k_x}{k^2} = \overline{U} k, \tag{24}$$

where we have $k_y = 2\pi/3500$ km^{-1}. The resulting value $L_x = 2\pi/k_x$ is compared with the numerically obtained one L_x^o in Table 2. The excellent numerical agreement, to within 5% of the value predicted by the theory, depends on the exact choice of normalization constant for L_x^o. But the order of magnitude is

clearly correct and L_x^o does increase with the intensity T_* of the forcing, and hence with $\overline{U}$, as predicted by the theory.

5.3 Intraseasonal variability of the jet

The dependence of the atmospheric dynamics was studied systematically as a function of the corrected strength T_* of the oceanic thermal front. The correction was used in the numerical part of the study in order to make the results of this part, at a given horizontal resolution, more directly comparable to the analytical results. For orientation purposes, T_* = 7 °C corresponds roughly to the strength of the Gulf Stream and Kuroshio surface fronts, when the frontal-width parameter in Eqs. (18) (infinite front) or (22) (finite front) is d = 50 km.

We found that for weak fronts ($T_* \leq$ 4 °C) the circulation is steady. This circulation has two large antisymmetric gyres with an eastward jet flowing between them (Fig. 8*a*). As the frontal strength increases (4 °C $\leq T_* \leq$ 5°C), the solution becomes periodic in time and asymmetric in space. The period is about 30 days. The asymmetry of the solution is the result of the symmetric pattern of the unstable oscillatory mode being superimposed on the antisymmetric pattern of the steady state that loses its stability (Figs. 8b and 9). This symmetric oscillatory mode has a wavelength of 1500 km. Its amplitude is the largest where the mean jet has its maximum speed, at y = 0. The jet's instability is due to the strong shear near the oceanic front.

When the front's intensity is increased to T_* = 5 °C, the solution becomes chaotic. For T_* > 6 °C the prominent period is 65–74 days. As T_* increases the intensity, as well as the spatial scale of both the mean and the anomaly, increase. For instance, for T_* = 7 °C the scale of the symmetric mode is 2000 km x 2000 km. The dependence of the solution on the zonal length of the oceanic front and the AMBL's parameters are left for further study, as is the response of a baroclinic free atmosphere to an oceanic thermal front.

5.4 Ultra-low-frequency atmospheric variability

Interdecadal and interannual variability in mid-latitude SSTs has been shown to exist in the North Atlantic and North Pacific (Bjerknes 1964; Deser and Blackmon 1993; Kushnir 1994). The influence of this variability on the atmosphere, or the interaction between the atmospheric and oceanic variability on these time scales, are not well understood.

We suggest here a possible mechanism for the influence of ultra-low-frequency variability in mid-latitude oceanic fronts on atmospheric LFV. Varying the intensity of the model's SST front with an interannual period led to periodic behavior in its free atmosphere with the same period (Figs. 11 and 12). The varying frontal strength induced an increase or decrease in the mean atmospheric jet's speed. Two regimes alternated over the period of the forcing: (1) When the oceanic front and the atmospheric jet are both strong, a high-energy regime is obtained. Large meanders and eddies develop along the jet axis, and the dominant oscillation has a period of about 70 days. (2) When the oceanic front and the atmospheric jet are both weak a low-energy regime results. In that regime small meanders develop along the jet axis, and the dominant oscillation has a period of about 30 days (Fig. 13).

The mechanism demonstrated in this paper for spinning up the circulation in the free atmosphere is not included in general circulation models (GCMs); this is mainly due to the atmospheric GCMs' low horizontal resolution, with a mesh size larger than 100 km. Since oceanic fronts have a width of about 100 km or less, they cannot be resolved by these models.

We suggest that the interannual and interdecadal variability of oceanic thermal fronts, such as that of the Gulf Stream and the Kuroshio Extension, can influence the atmospheric flow above through the thermal pumping of the intervening AMBL. The main computational obstacle for exploring further the mechanism found here in large-scale GCMs is the fine horizontal resolution needed to resolve the

fronts. One way to overcome this obstacle is to use nested grids, with high resolution over the region of major oceanic fronts and low resolution elsewhere.

Acknowledgements. It is a pleasure to thank Sandra Topete-Hernandez for help in editing the paper and facilitating communication between the three co-authors on three continents. This work was supported by a Senior Visiting Fellowship of UCLA's Center for Earth System Research (YF), NSF grant ATM00-82131 (YF and MG), and DOE grant DOE DE-FG02-01ER63251 (MG and ES)

References

Batchelor, G. K., 2000: *An Introduction to Fluid Dynamics*, Cambridge University Press, 615 pp.

Bjerknes, J., 1964: Atlantic air-sea interaction. *Adv. Geophys.*, **10**, 1–82.

Branstator, G. W., 1987: A striking example of the atmosphere's leading traveling pattern. *J. Atmos. Sci.*, **44**, 2310–2323.

Businger, J. A. and W. J. Shaw, 1984: The response of the marine boundary layer to mesoscale variations in sea-surface temperature. *Dyn. Atmos. Oceans*, **8**, 267–281.

Chao, Y., M. Ghil, and J. C. McWilliams, 2000: Pacific interdecadal variability in this century's sea surface temperatures, *Geophys. Res. Lett.*, **27**, 2261–2264.

Charney, J. G., 1971: Geostrophic turbulence. *J. Atmos. Sci.*, **28**, 1087–1095.

Chen, Z.-M., M. Ghil, and S. Wang, 2002: Hopf bifurcation in quasi-geostrophic channel flow, *SIAM J. Appl. Math., sub judice*.

Deser, C., and M.L. Blackmon, 1993: Surface climate variations over the North Atlantic ocean during winter: 1900–1989. *J. Climate,* **6**, 1743–1753.

Dickey, J. O., M. Ghil, and S. L. Marcus, 1991: Extratropical aspects of the 40–50 oscillation in length-of-day and atmospheric angular momentum, *J. Geophys. Res.*, **96**, 22643–22658.

Doyle, J. D. and T. T. Warner, 1990: Mesoscale coastal processes during GALE IOP-2. *Mon. Wea. Rev.*, **118**, 283–308.

Doyle, J. D. and T. T. Warner, 1993: Nonhydrostatic simulations of coastal mesobeta-scale vortices and frontogenesis., *Mon. Wea. Rev.*, **121**, 3371–3392.

Feliks, Y., 1990: Isolated vortex evolution in 2 and 4 mode models . *Deep-Sea Res.*, **37**, 571–591.

Feliks, Y. and M. Ghil, 1996: Mixed barotropic-baroclinic eddies growing on an eastward midlatitude jet. *Geophys. Astrophys. Fluid Dyn.*, **82**, 137–171.

Gallego, B. and P. Cessi, 2001: Decadal variability of two oceans and an atmosphere. *J. Clim.*, **13**, 2815–2832.

Ghil, M., and Mo, K.-C., 1991a: Intraseasonal oscillations in the global atmosphere. Part I: Northern hemisphere and tropics, *J. Atmos. Sci.*, **48**, 752–779.

Ghil, M., and K.-C. Mo, 1991b: Intraseasonal oscillations in the global atmosphere. Part II: Southern Hemisphere, *J. Atmos. Sci.*, **48**, 780–790.

Ghil, M., and A. W. Robertson, 2000: Solving problems with GCMs: General circulation models and their role in the climate modeling hierarchy. *General Circulation Model Development: Past, Present and Future,* D. Randall (Ed.), Academic Press, San Diego, pp. 285–325.

Ghil, M., M. R. Allen, M. D. Dettinger, K. Ide, D. Kondrashov, M. E. Mann, A. W. Robertson, A. Saunders, Y. Tian, F. Varadi, and P. Yiou, 2002: Advanced spectral methods for climatic time series*, Rev. Geophys.*, 10.1029/2000GR000092, in press.

Giordani, H., and S. Planton, 2000: Modeling and analysis of ageostrophic circulation over the Azores oceanic front during the SEMAPHORE experiment. *Mon. Wea. Rev.*, **128**, 2270–2287.

Haidvogel, D.B., A.R. Robinson, and E.E. Schulman, 1980: The accuracy, efficiency and stability of three numerical models with application to open ocean problems. *J. Comput. Phys.*, **34**, 1–53.

Haltiner, G.J., and R.T. Williams, 1979: *Numerical Prediction and Dynamic Meteorology,* 2nd ed. John Wiley & Sons, New York/ Chichester/ Brisbane/ Toronto/ Singapore, 477 pp.

Holton, J. R., 1992: *An Introduction to Dynamic Meteorology*, 3rd ed. Academic Press, San Diego, 511 pp.

Hsu, H., 1987: Study of linear steady atmospheric flow above a finite surface heating. *J. Atmos. Sci.*, **44**, 186–199.

Jiang, S., F.-F. Jin, and M. Ghil, 1995: Multiple equilibria, periodic, and aperiodic solutions in a wind-driven, double-gyre, shallow-water model. *J. Phys. Oceanogr.*, **25**, 764–786.

Jin, F-F., and M. Ghil, 1990: Intraseasonal oscillations in the extratropics: Hopf bifurcation and topographic instabilities, *J. Atmos. Sci.*, **47**, 3007–3022.

Jin, F.-F., J. D. Neelin and M. Ghil, 1994: El Niño on the Devil's Staircase: Annual subharmonic steps to chaos, *Science*, **264**, 70–72.

Jin, F.-F., J. D. Neelin, and M. Ghil, 1996: El Niño/Southern Oscillation and the annual cycle: Subharmonic frequency-locking and aperiodicity. *Physica D*, **98**, 442–465.

Keppenne, C. L., S. Marcus, M. Kimoto, and M. Ghil, 2000: Intraseasonal variability in a two-layer model and observations, *J. Atmos. Sci.,* **57**, 1010–1028.

Kuo, H.L., 1973: Dynamics of quasi-geostrophic flows and instability theory. *Adv. Appl. Mech.*, **13**, 247–330.

Kushnir, Y., 1987: Retrograding wintertime low-frequency disturbances over the North Pacific Ocean. *J. Atmos. Sci.*, **44**, 2727–2742.

Kushnir, Y., 1994: Interdecadal variations in North Atlantic sea surface temperature and associated atmospheric conditions, *J. Clim*., **7**, 141–157.

Lee, T., and P. Cornillon, 1996: Propagation of Gulf Stream meanders between 74^0 and 70^0W, *J. Phys. Oceanogr*., 26, 205–224.

Lott, F., A. W. Robertson, and M. Ghil, 2001: Mountain torques and atmospheric oscillations. *Geophys. Res. Lett*., **28**, 1207–1210.

Madden, R. A., and P. R. Julian, 1971: Detection of a 40-50 day oscillation in the zonal wind in the Tropical Pacific. *J. Atmos. Sci.*, **28**, 702-708.

Madden, R. A., and P. R. Julian, 1994: Observations of the 40–50 day tropical oscillation—A review, *Mon. Wea. Rev*., **122**, 814–837.

Moron, V., R. Vautard, and M. Ghil, 1998: Trends, interdecadal and interannual oscillations in global sea-surface temperatures. *Clim. Dyn.,* **14**, 545–569.

Neelin, J. D., and W. Weng, 1999: Analytical prototypes for ocean–atmosphere interaction. Part I: Coupled feedbacks as a sea surface temperature dependent stochastic process. *J. Clim*., **12**, 697–721.

Pedlosky, J., 1987: *Geophysical Fluid Dynamics,* 2nd ed. Springer-Verlag, New York/Heidelberg/Berlin, 710 pp.

Plaut, G., and R. Vautard, 1994: Spells of low-frequency oscillations and weather regimes in the Northern Hemisphere. *J. Atmos. Sci.*, **51**, 210–236.

Rhines, P .B., 1975: Waves and turbulence on a beta-plane. *J. Fluid Mech*., **69**, 417–443.

Robertson, A. W., M. Ghil, and M. Latif, 2000: Interdecadal changes in atmospheric low-frequency variability with and without boundary forcing, *J. Atmos. Sci.,* **57**, 1132–1140.

Robinson, A. R. (Ed.), 1983: *Eddies in Marine Science*, Springer-Verlag, Berlin/Heidelberg/New York/Tokyo, 609 pp.

Rogers, D. P., 1989: The marine boundary layer in vicinity of an ocean front. *J. Atmos. Sci*., **46**, 2044–2062.

Salmon R., 1998: *Lectures on Geophysical Fluid Dynamics*. Oxford Univ. Press, New York/Oxford, 378 pp.

Saravanan, R., and J. C. McWilliams, 1995: Multiple equilibria, natural variability, and climate transitions in an idealized ocean-atmosphere model. *J. Clim.*, **8**, 2296–2323.

Shapiro, R., 1970: Smoothing, filtering, and boundary effects. *Rev. Geophys. Space Phys.*, **8**, 359–387.

Simmons, A. J., J. M. Wallace, and G. W. Branstator, 1983: Barotropic wave propagation and instability, and atmospheric teleconnection patterns. *J. Atmos. Sci.*, **40**, 1363–1392.

Stommel, H. M., 1965: *The Gulf Stream: A Physical and Dynamical Description.* 2d ed., University of California Press, Berkeley, 248 p.

Stommel, H. M., and Kozo Yoshida (Eds.), 1972: *Kuroshio: Physical Aspects of the Japan Current*. University of Washington Press, Seattle, 517 p.

Speich, S., H. Dijkstra, and M. Ghil, 1995: Successive bifurcations in a shallow-water model, applied to the wind-driven ocean circulation, *Nonlin. Proc. Geophys.,* **2**, 241–268.

Strong, C. M., F.-F. Jin and M. Ghil, 1993: Intraseasonal variability in a barotropic model with seasonal forcing, *J. Atmos. Sci.*, **50**, 2965–2986.

Strong, C. M., F.-F. Jin and M. Ghil, 1995: Intraseasonal oscillations in a barotropic model with annual cycle, and their predictability, *J. Atmos. Sci.*, **52**, 2627–2642.

Sweet, W., R. Fett, J. Kerling and P. LaViolette, 1981: Air-sea interaction effects in the lower troposphere across the north wall of the Gulf Stream. *Mon. Wea. Rev.*, **109**, 1042–1052.

Tziperman, E., L. Stone, M. Cane and H. Jarosh, 1994: El Niño chaos: Overlapping of resonances between the seasonal cycle and the Pacific ocean–atmosphere oscillator, *Science*, **264**, 72–74.

Warner, T. T., M. N. Lakhtakia, J. D. Doyle, and R. A. Pearson, 1990: Marine atmospheric boundary layer circulations forced by Gulf Stream sea surface temperature gradients. *Mon. Wea. Rev.*, **118**, 309–323.

Weng, W., and J.D. Neelin, 1999: Analytical prototypes for ocean–atmosphere interaction at mid-latitudes. Part II: Mechanisms for coupled gyres modes. *J. Clim.*, **12**, 2757–2774.

Table 1: Characteristic scales for the atmospheric model.

L (km)	50
H (km)	10
H_a (km)	7.8
H_E (km)	0.81
T_i (day)	0.58
V (ms^{-1})	1
β_0 ($m^{-1}\ s^{-1}$)	$1.8 \cdot 10^{-11}$
k ($m^2 s^{-1}$)	3.3
k_H ($m^2 s^{-1}$)	10^2
f (s^{-1})	10^{-4}
g (ms^{-2})	9.81
θ_0 (^{0}K)	300
ρ_0 (gcm^{-3})	10^{-3}

Table 2. Dependence of the atmospheric jet's penetration length on the oceanic front's intensity.

T_*	$\overline{U}\,(\mathrm{ms}^{-1})$	$\overline{U}_{\max}(\mathrm{ms}^{-1})$	$k_x\,(\mathrm{km}^{-1})$	$L_x = \frac{2\pi}{k_x}(\mathrm{km})$	$L_x^o(\mathrm{km})$
5	1.1	7.5	$3.3\cdot10^{-3}$	1900	1850
6	1.3	8.3	$2.9\cdot10^{-3}$	2140	2150
7	1.4	9.2	$2.7\cdot10^{-3}$	2330	2450

$\overline{U}$ is the solution's root-mean-square velocity, $\overline{U}_{\max}$ is the maximum speed of the jet, and k_x is zonal wavelength; the last two columns compare the theoretical length L_x with the numerically obtained one L_x^o. The value of k_x in the table corresponds to the largest one that is consistent with Eq. (24).

List of figures

Fig. 1: The prescribed SST pattern for a finite-length front with strength T_a = 3.5°C and frontal-width parameter d = 50 km; see Eq. (22). Contour interval (CI) is 2 °C, starting at ±1 °C; positive contours are solid, negative and zero contours dashed. The front lies along the x-axis, is 600 km long and is centered at x = 1000 km. All spatial patterns are shown for the same rectangular domain of 4000 km x 3500 km.

Fig. 2: Cross-sections of the oceanic and atmospheric fronts along the y-axis for an infinite oceanic front with frontal strength T_a = 1 °C and frontal width d = 50 km; see Eq. (18). (a) The prescribed SST profile; (b) the vertical velocity at the top of the AMBL.

Fig. 3: The analytically obtained vertical profile of u (solid) and v (dashed) in the AMBL, at y = 0.

Fig. 4: Different terms in the AMBL momentum equation, Eq. (4b), and the omitted nonlinear term, for an infinite oceanic front: pressure term $-(1/\rho)(\partial p/\partial y)$ (solid), diffusion term $k\partial^2 v/\partial z^2$ (dashed), Coriolis term fu (dash-dotted), and cross-frontal advection term $v(\partial v/\partial y)$ (triple-dotted). The vertical profiles at y = 30 km: (a) weak front, T_a = 1 °C; and (b) strong front, T_a = 3.5 °C. The cross-front profiles (along the y-axis), at z = 225 m: (c) weak front; and (d) strong front.

Fig. 5: The analytically obtained meridional, cross-front profile of the zonal, along-front velocity $u_G = u_G(y)$, for T_a = 1 °C.

Fig. 6: The numerically obtained free-atmosphere streamfunction (nondimensioanl) for a finite-length oceanic front. Snapshots shown at unequally spaced times, for a spin-up experiment carried out at the adjusted frontal strength T_* = 7 °C; CI = 2. The adjustment factor A in $T_* = AT_a$ is given by Eq. (21) and equals 2.06.

Fig. 7: The 68-day oscillation. (a) The power spectrum of the mean kinetic energy density of the atmospheric jet, computed over a subdomain $\{0 \leq x \leq 80, -1 \leq y \leq 1\}$ (in nondimensional units) as the integral of $\nabla\psi^2$ divided by the area. (b) The 68-day oscillation obtained at $T_* = 7$ °C is reconstructed using the leading pair of modes and plotted at 8 equidistant phases. The plots show the anomalous streamfunction, i.e., the difference between the field in the corresponding phase and the mean over the oscillation; phase 1 is in the upper left panel and CI = 1 nondimensional unit.

Fig. 8: Model streamfunction fields for increasing strength T_* of the finite-length oceanic front: a) steady-state solution for $T_* = 4$ °C; (b)–(d) the mean streamfunction for — (b) $T_* = 4.5$ °C; (c) $T_* = 6$ °C; and (d) $T_* = 7$ °C; CI = 2.4 nondimensional units.

Fig. 9: The spatially symmetric component of the 31-day oscillatory mode at 4 equally spaced epochs during a half period for $T_* = 4.5$ °C; CI = 1 nondimensional unit.

Fig. 10: The symmetric component (left panels) and the antisymmetric component (right panels) of the 74-day mode, at two different times, 37 days apart, in the chaotic regime obtained for $T_* = 6$ °C. CI = 1 nondimensional unit.

Fig. 11: The evolution of the periodically forced flow. (a) The kinetic energy over the integration domain as a function of time; only 3 complete cycles of the 7-year forcing are shown. (b, c) Streamfunction field for the (b) low-energy phase of the forced solution, at $t = 3153$; and (c) high-energy phase, at $t = 5834$. CI = 2 nondimensional unit.

Fig. 12: The reconstructed 7-year oscillation in 8 phases. Phase 1 is the upper-left panel and CI = 1 nondimensional unit.

Fig. 13: Evolutive power spectrum of the model's ultra-low-frequency behavior: time-frequency diagram (upper panel) of the streamfunction time series at grid location (45,0) (lower panel). The

modulus of the short-time Fourier transform $\left| \int x(s)h^{*}(s-t)e^{-2\pi i\nu s}ds \right|$ in the upper panel has been computed using a Gaussian window $h(s)$ with a width parameter of 4 years that favors frequency resolution vs. time resolution in the Heisenberg-principle trade-off; here $x(t)$ is the time series being analyzed, $h^{*}(s)$ is the complex conjugate of $h(s)$, i is the imaginary unit, and ν the frequency. The streamfunction in the lower panel is given the nondimensional units.

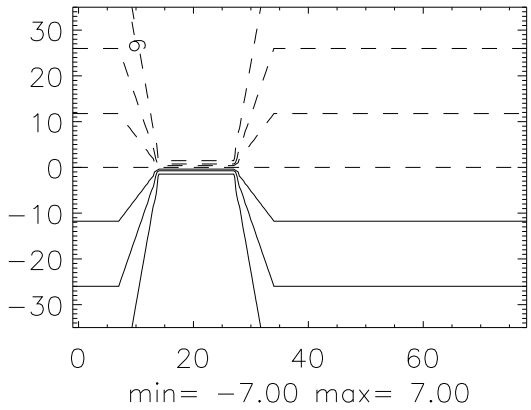
30
20
10
0
−10
−20
−30
0
20
40
60
min= −7.00 max= 7.00

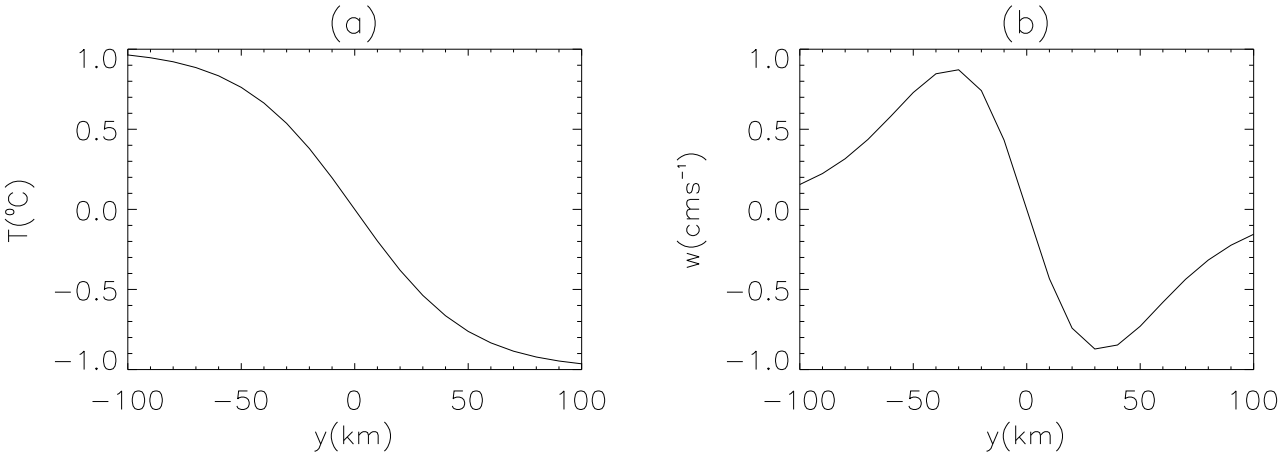
(a)
1.0
0.5
0.0
−0.5
−1.0
T(°C)
−100
−50
0
50
100
y(km)
(b)
1.0
0.5
0.0
−0.5
−1.0
w(cms^{-1})
−100
−50
0
50
100
y(km)

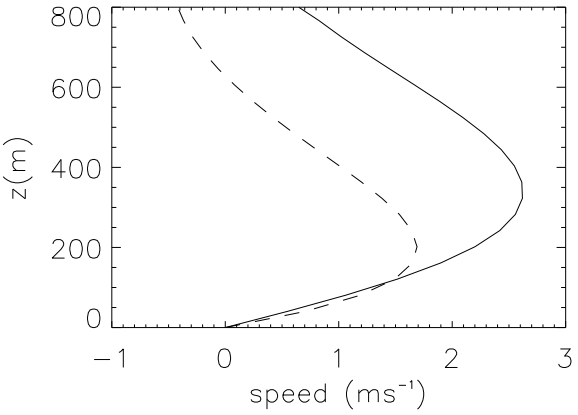
800
600
400
200
0
z(m)
−1
0
1
2
3
speed (ms⁻¹)

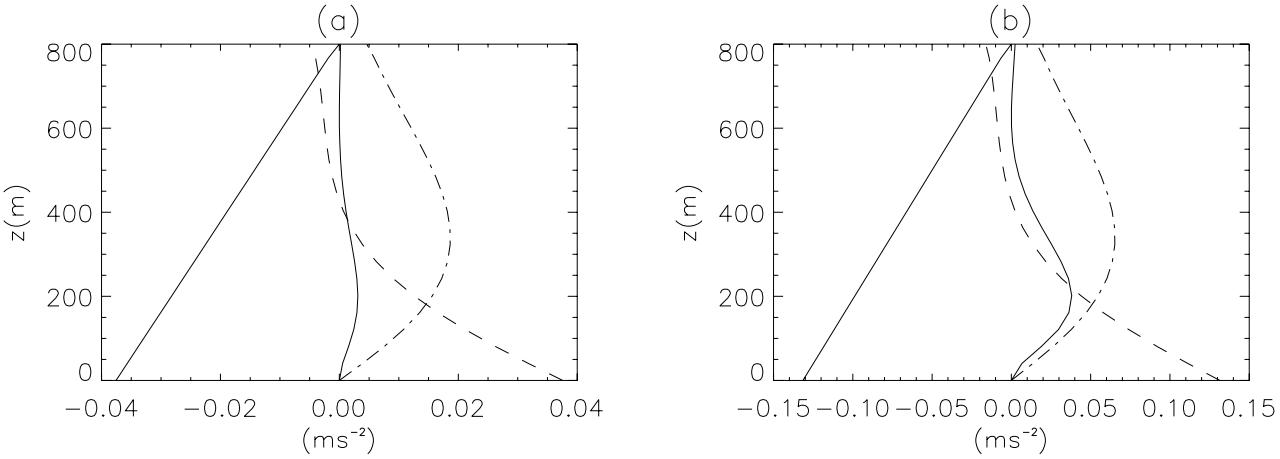
(a)
800
600
400
200
0
z(m)
−0.04
−0.02
0.00
0.02
0.04
(ms⁻²)
(b)
800
600
400
200
0
z(m)
−0.15
−0.10
−0.05
0.00
0.05
0.10
0.15
(ms⁻²)

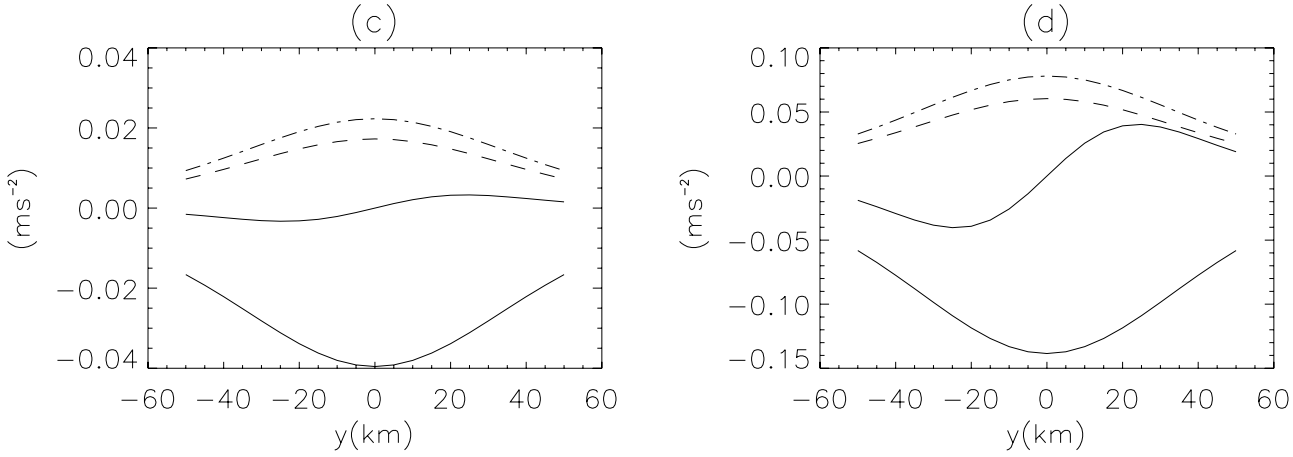
(c)
0.04
0.02
0.00
−0.02
−0.04
(ms⁻²)
−60
−40
−20
0
20
40
60
y(km)
(d)
0.10
0.05
0.00
−0.05
−0.10
−0.15
(ms⁻²)
−60
−40
−20
0
20
40
60
y(km)

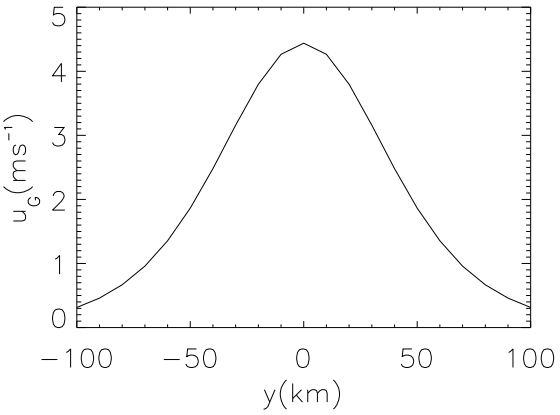
5
4
3
2
1
0
$u_G(ms^{-1})$
−100
−50
0
50
100
y(km)

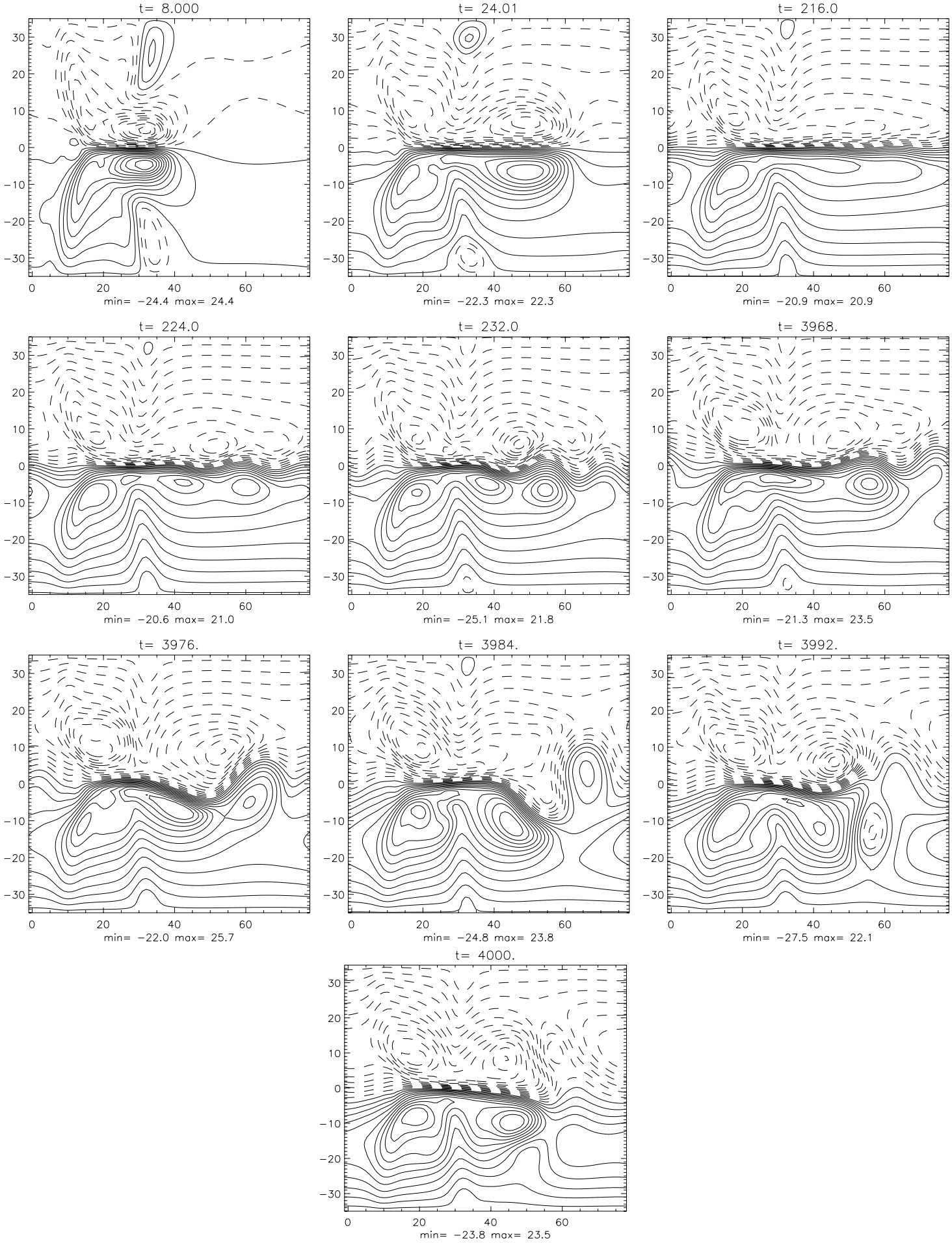
t= 8.000
min= −24.4 max= 24.4
t= 24.01
min= −22.3 max= 22.3
t= 216.0
min= −20.9 max= 20.9
t= 224.0
min= −20.6 max= 21.0
t= 232.0
min= −25.1 max= 21.8
t= 3968.
min= −21.3 max= 23.5
t= 3976.
min= −22.0 max= 25.7
t= 3984.
min= −24.8 max= 23.8
t= 3992.
min= −27.5 max= 22.1
t= 4000.
min= −23.8 max= 23.5

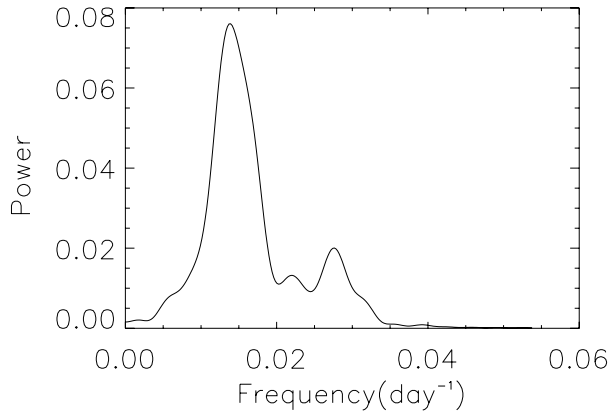
0.08
0.06
0.04
0.02
0.00
Power
0.00
0.02
0.04
0.06
Frequency(day^{-1})

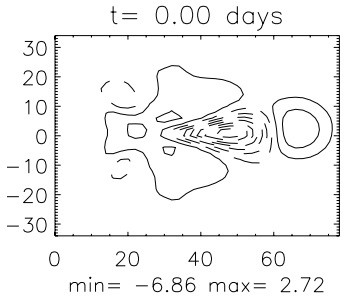
t= 0.00 days
30
20
10
0
−10
−20
−30
0
20
40
60
min= −6.86 max= 2.72

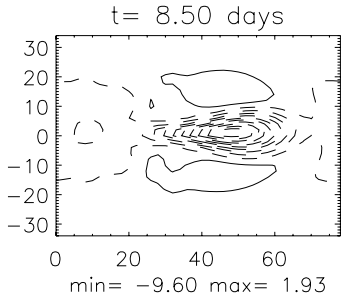
t= 8.50 days
30
20
10
0
−10
−20
−30
0
20
40
60
min= −9.60 max= 1.93

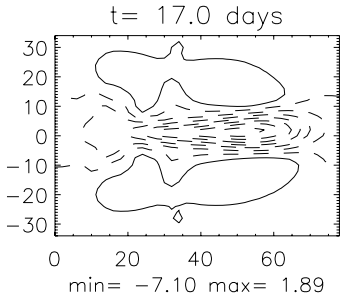
t= 17.0 days
30
20
10
0
−10
−20
−30
0
20
40
60
min= −7.10 max= 1.89

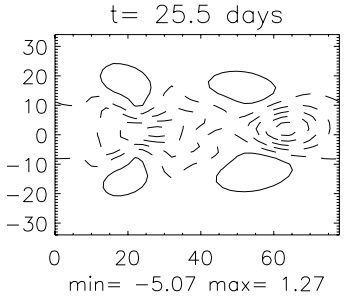
t= 25.5 days
30
20
10
0
−10
−20
−30
0
20
40
60
min= −5.07 max= 1.27

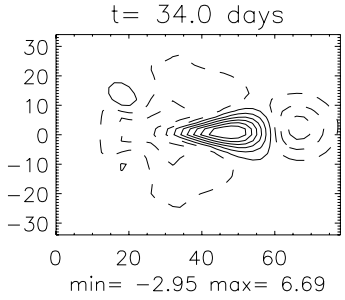
t= 34.0 days
30
20
10
0
−10
−20
−30
0
20
40
60
min= −2.95 max= 6.69

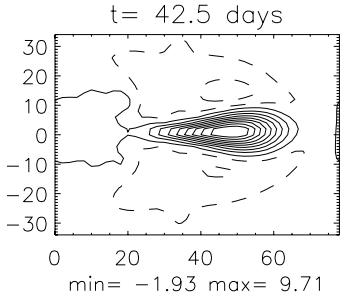
t= 42.5 days
30
20
10
0
−10
−20
−30
0
20
40
60
min= −1.93 max= 9.71

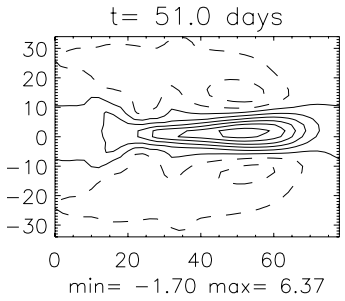
t= 51.0 days
30
20
10
0
−10
−20
−30
0
20
40
60
min= −1.70 max= 6.37

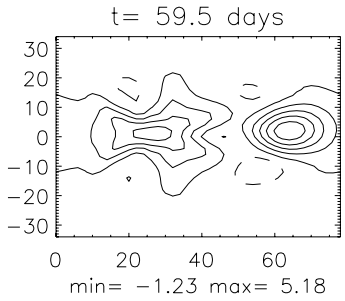
t= 59.5 days
30
20
10
0
−10
−20
−30
0
20
40
60
min= −1.23 max= 5.18

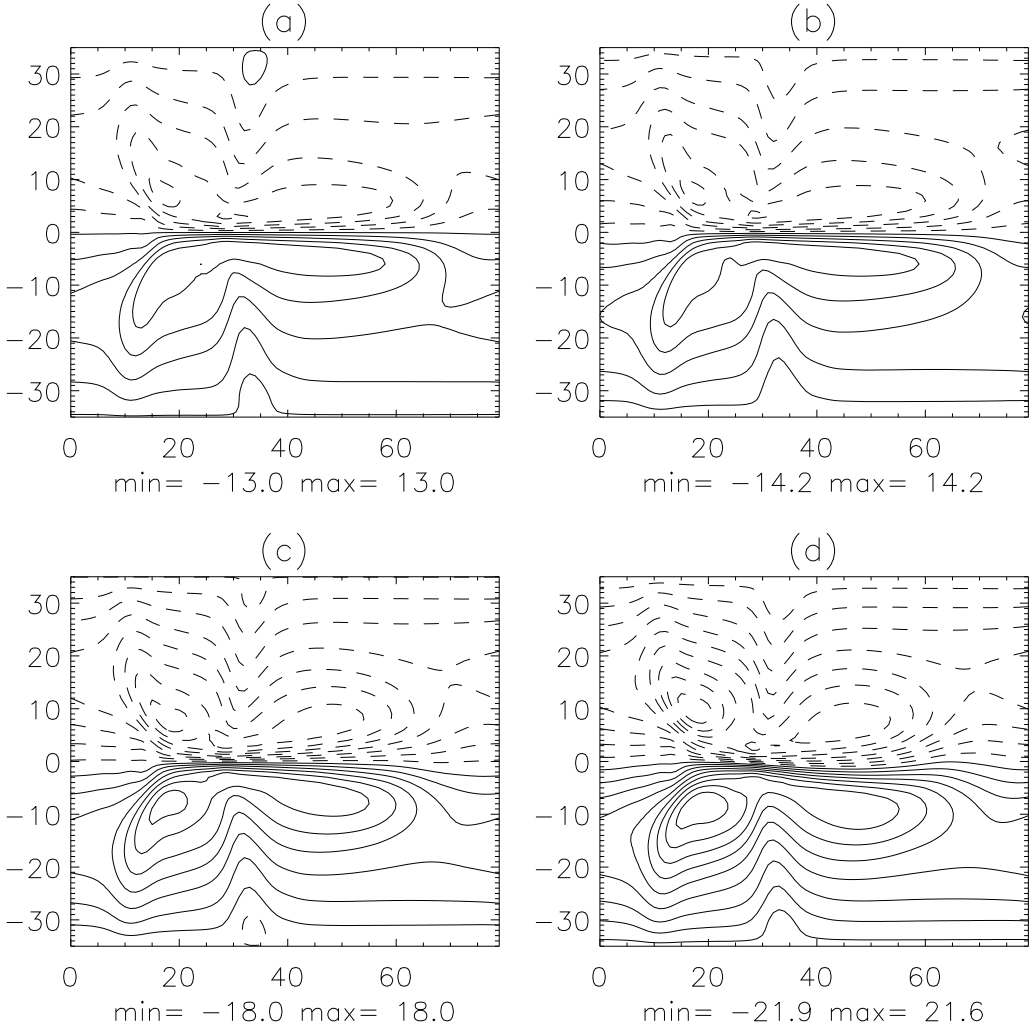
(a)
(b)
(c)
(d)
30
20
10
0
−10
−20
−30
0
20
40
60
min= −13.0 max= 13.0
min= −14.2 max= 14.2
min= −18.0 max= 18.0
min= −21.9 max= 21.6

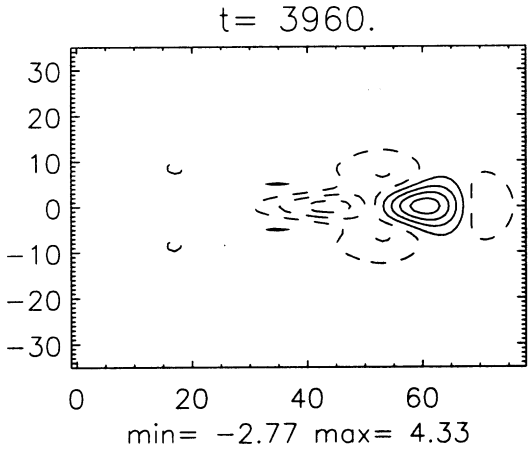
t= 3960.
30
20
10
0
−10
−20
−30
0
20
40
60
min= −2.77 max= 4.33

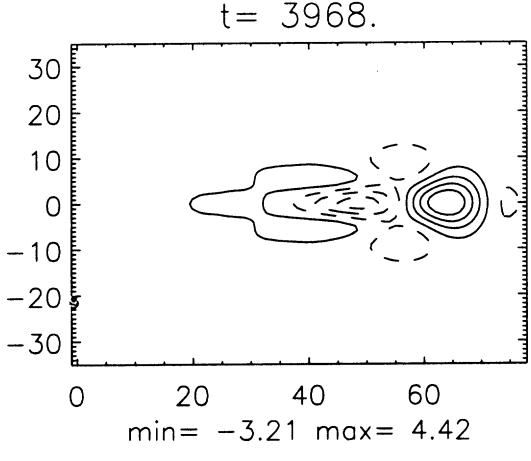
t= 3968.
30
20
10
0
−10
−20
−30
0
20
40
60
min= −3.21 max= 4.42

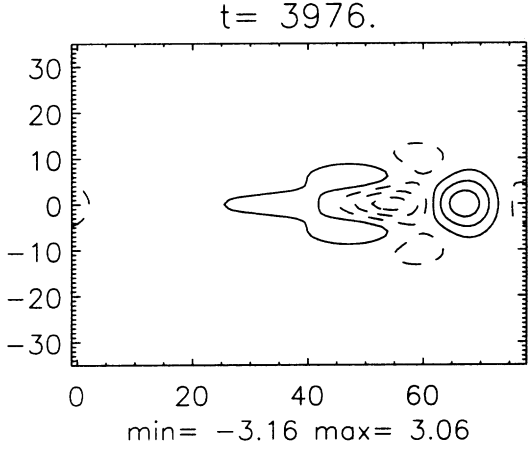
t= 3976.
30
20
10
0
−10
−20
−30
0
20
40
60
min= −3.16 max= 3.06

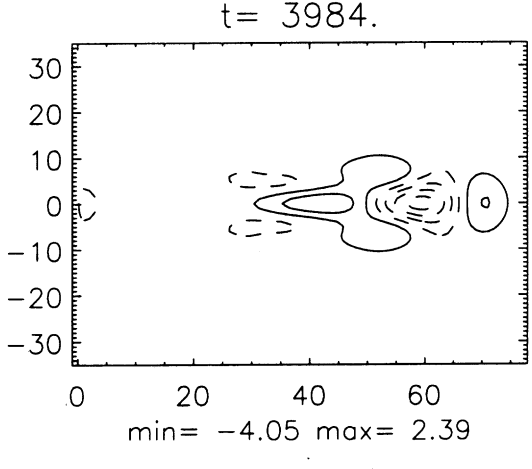
t= 3984.
30
20
10
0
−10
−20
−30
0
20
40
60
min= −4.05 max= 2.39

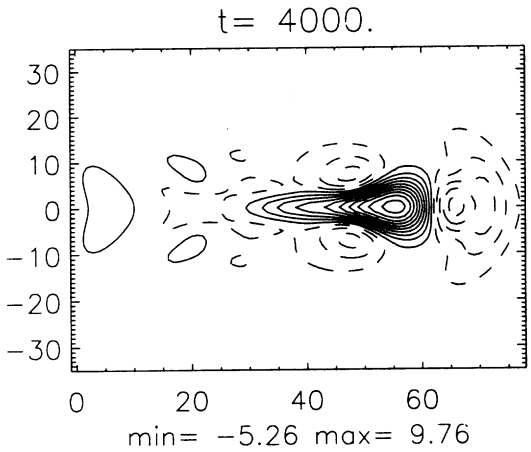
t= 4000.
30
20
10
0
−10
−20
−30
0
20
40
60
min= −5.26 max= 9.76

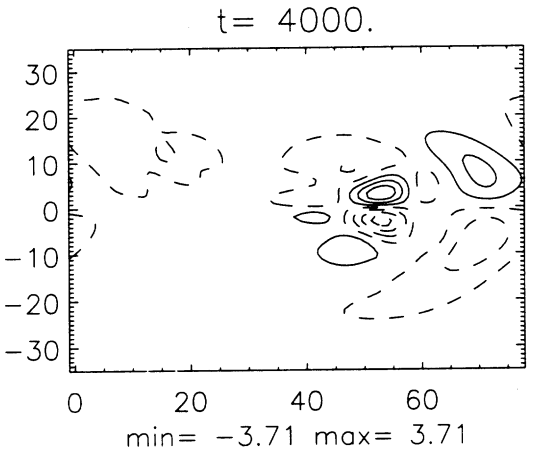
t= 4000.
30
20
10
0
−10
−20
−30
0
20
40
60
min= −3.71 max= 3.71

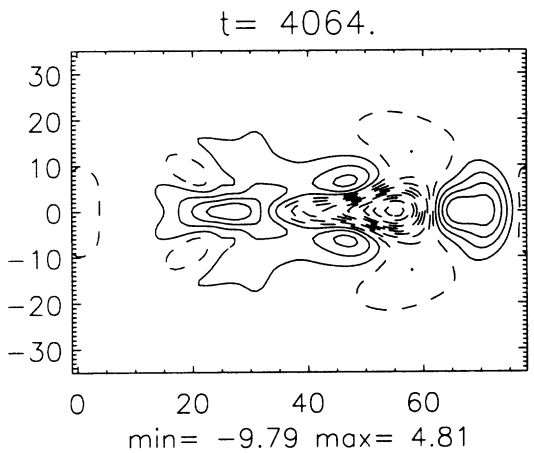
t= 4064.
30
20
10
0
−10
−20
−30
0
20
40
60
min= −9.79 max= 4.81

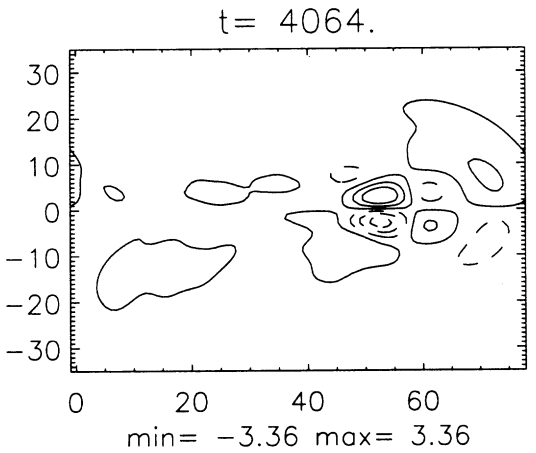
t= 4064.
30
20
10
0
−10
−20
−30
0
20
40
60
min= −3.36 max= 3.36

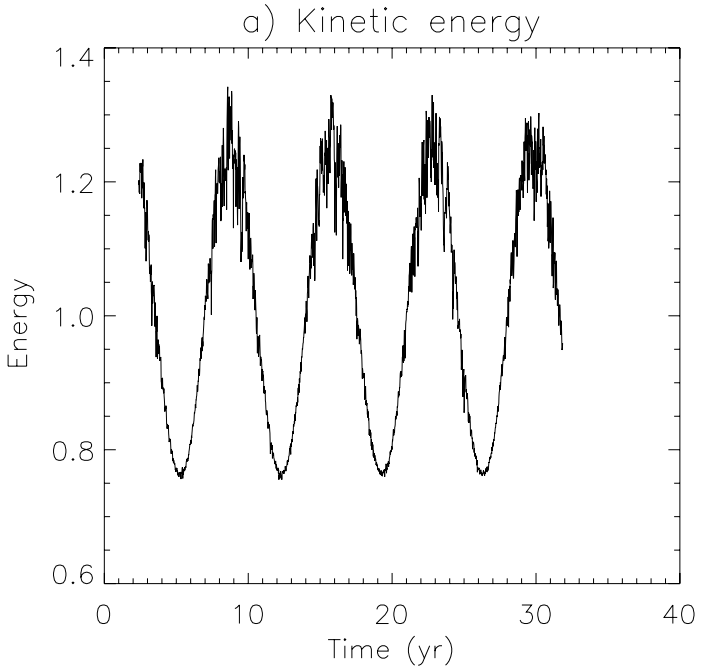
a) Kinetic energy
1.4
1.2
1.0
0.8
0.6
Energy
0
10
20
30
40
Time (yr)

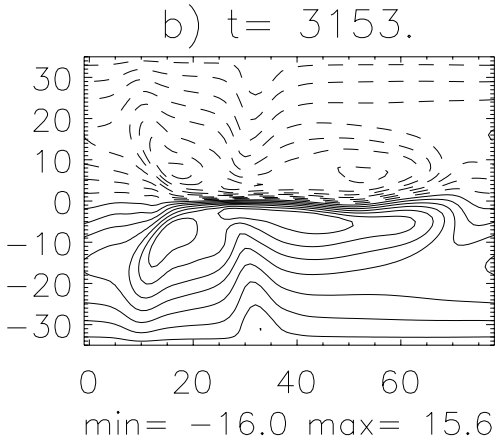
b) t= 3153.
30
20
10
0
−10
−20
−30
0
20
40
60
min= −16.0 max= 15.6

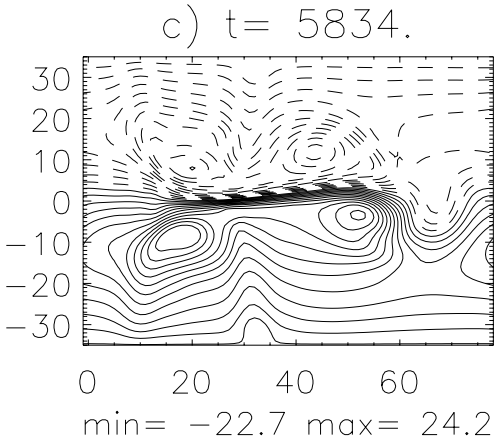
c) t= 5834.
30
20
10
0
−10
−20
−30
0
20
40
60
min= −22.7 max= 24.2

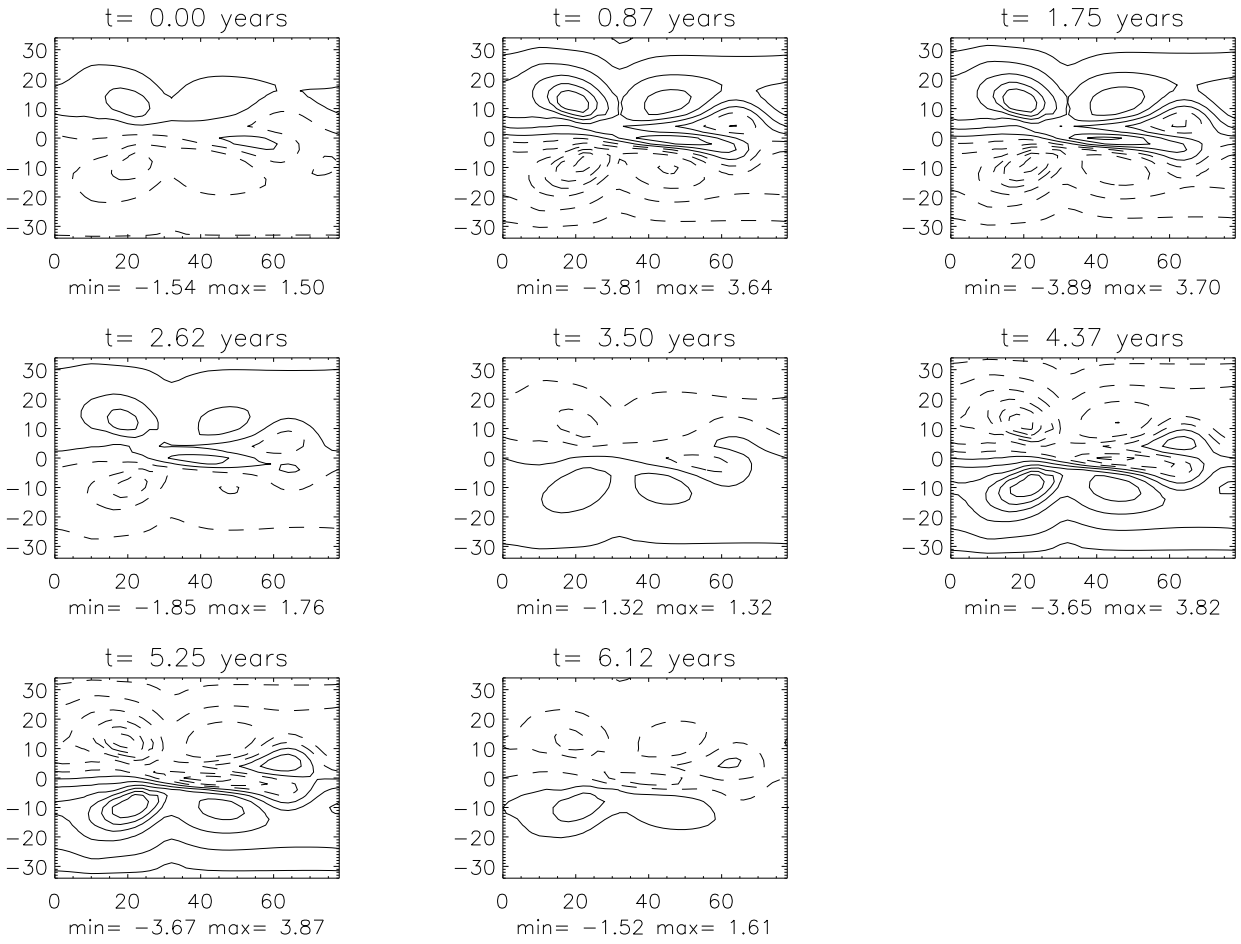
t= 0.00 years
min= −1.54 max= 1.50
t= 0.87 years
min= −3.81 max= 3.64
t= 1.75 years
min= −3.89 max= 3.70
t= 2.62 years
min= −1.85 max= 1.76
t= 3.50 years
min= −1.32 max= 1.32
t= 4.37 years
min= −3.65 max= 3.82
t= 5.25 years
min= −3.67 max= 3.87
t= 6.12 years
min= −1.52 max= 1.61

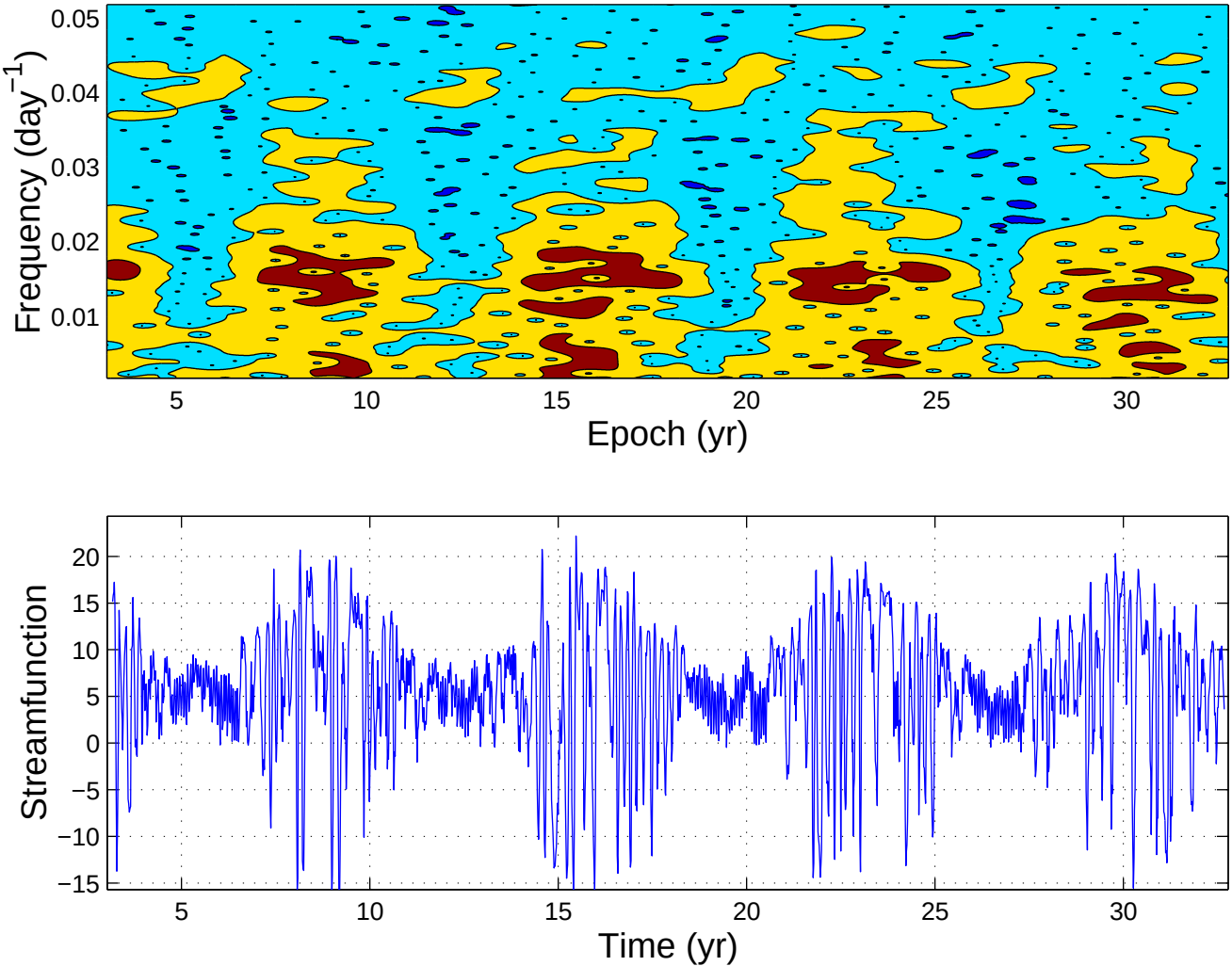
Frequency (day^{-1})
0.05
0.04
0.03
0.02
0.01
5
10
15
20
25
30
Epoch (yr)
Streamfunction
20
15
10
5
0
−5
−10
−15
5
10
15
20
25
30
Time (yr)